International Journal of Nanomedicine

Dovepress
Taylor & Francis Group

Open Access Full Text Article

ORIGINAL RESEARCH

Regulation of Neuroimmune Microenvironment by PLA/GO/Anti-TNF-α Composite to Enhance Neurological Repair After Spinal Cord Injury

Yishu Liu[1–3], Jingsong Liu[1–3], Yangyang Wang[1–3], Yubo Zhang[1–3], Zhibin Peng[1–3], Pengfei Li[1–3], Mi Li[1–3], Bing Xue[4], Yansong Wang[1–3,5]

[1]Department of Orthopedics, The First Affiliated Hospital of Harbin Medical University, Harbin, Heilongjiang, People's Republic of China; [2]The Key Laboratory of Myocardial Ischemia, Ministry of Education, Harbin Medical University, Harbin, Heilongjiang, People's Republic of China; [3]State Key Laboratory of Frigid Zone Cardiovascular Diseases, Harbin Medical University, Harbin, Heilongjiang, People's Republic of China; [4]Department of Orthopedics, The Second Affiliated Hospital of Harbin Medical University, Harbin, Heilongjiang, People's Republic of China; [5]NHC Key Laboratory of Cell Transplantation, Harbin Medical University, Harbin, Heilongjiang, People's Republic of China

Correspondence: Yansong Wang, Email wyshmu1975@163.com

Introduction: Spinal cord injury (SCI) is a severe neurological condition with limited treatment options. Polylactic acid (PLA)+graphene oxide (GO)+anti-TNF-α (Ab) composites have shown potential in regulating immune responses and promoting neural repair.

Methods: Electrospinning PLA+GO+Ab materials were characterized using scanning electron microscopy (SEM), Fourier-transform infrared spectroscopy (FTIR), X-ray photoelectron spectroscopy (XPS), Raman spectroscopy, and X-ray diffraction (XRD). Their effects on neural stem cells (NSCs) and macrophage polarization were evaluated through in vitro assays, including proliferation, migration, differentiation, and flow cytometry. A rat SCI model was used to assess motor function recovery and histological changes.

Results: PLA+GO+Ab promoted NSC proliferation, migration, and differentiation while inducing macrophage polarization toward the M2 phenotype, reducing inflammation. In the SCI model, PLA+GO+Ab treatment enhanced motor function recovery, reduced spinal cord damage, and promoted axonal regeneration and oligodendrocyte maturation. RNA sequencing identified activation of the Rap1 signaling pathway, contributing to these effects.

Discussion: PLA+GO+Ab composites effectively modulate the neuroimmune microenvironment, supporting SCI recovery by promoting neural repair and immune regulation. These findings suggest its potential as a therapeutic biomaterial for SCI treatment.

Keywords: spinal cord injury, nerve regeneration, graphene, polylactic acid, anti-tumor necrosis factor α, neuroimmunomodulation

Introduction

Spinal cord injury (SCI) is a severe trauma to the central nervous system characterized by high disability rates due to motor, secondary injuries may lead to further necrosis, swelling (peaking within 3–6 d and then gradually subsiding), and persistent inflammation and related damage.[1,2] Among these, the inflammatory response plays a crucial role in aggravating neuronal injury and impeding regeneration.

Tumor necrosis factor-alpha (TNF-α) is a key pro-inflammatory cytokine that mediates immune responses in SCI,[3] contributing to neuronal apoptosis, glial activation, and the recruitment of immune cells. Its persistent overexpression exacerbates tissue damage and creates an inhibitory microenvironment for neural repair. TNF-α is primarily produced by activated macrophages, microglia, and astrocytes at the injury site, and its interaction with TNF receptors initiates signaling cascades that activate nuclear factor-kappa B (NF-κB),[4] mitogen-activated protein kinases (MAPKs), and caspases, leading to increased inflammation, oxidative stress, and neuronal apoptosis. Elevated TNF-α levels also disrupt the blood-spinal cord barrier, allowing further infiltration of inflammatory cells and aggravating secondary damage. As an immunomodulator, TNF-α therapy has been proposed to manage SCI.[5–7] Therefore, targeting TNF-α through anti-TNF-α therapies represents a promising approach to mitigating inflammation and promoting functional recovery after SCI.

Received: 17 December 2024
Accepted: 14 April 2025
Published: 17 April 2025

Graphical Abstract

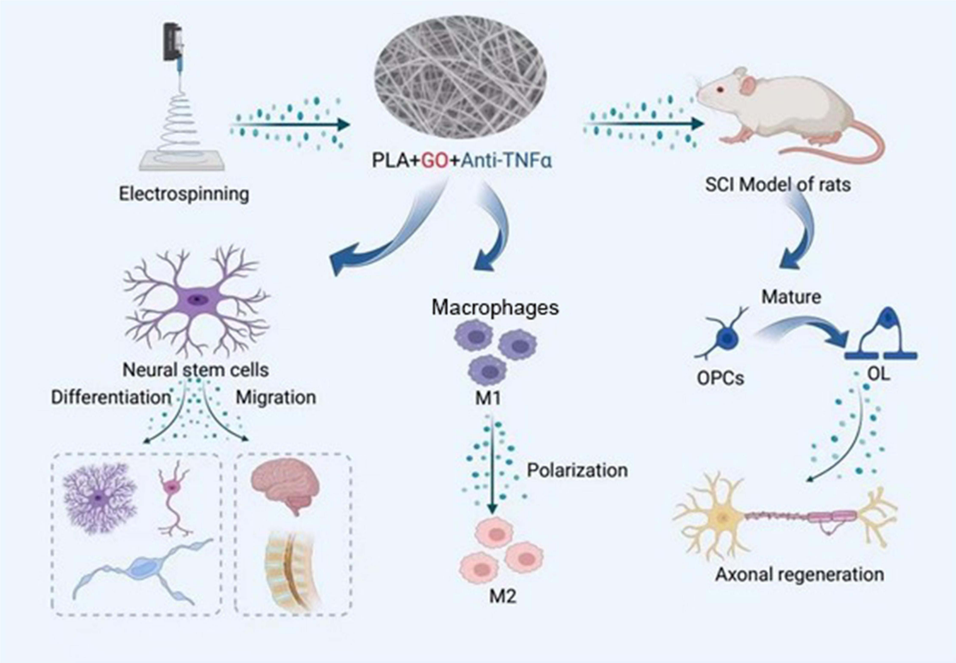

Current biomaterial-based strategies for SCI treatment include hydrogels, drug-eluting scaffolds, and bioengineered matrices.[8] These materials aim to provide structural support, modulate the immune response, facilitate neural regeneration, promote neural differentiation, and reduce inflammation.[9–11] While these approaches have shown some success, electrospinning offers unique advantages in scaffold fabrication. Electrospun nanofibrous scaffolds closely mimic the extracellular matrix, providing a highly porous, interconnected structure that supports cell adhesion, proliferation, and differentiation.[12,13] Among various biomaterials, graphene and graphene-based materials have emerged as promising candidates due to their ability to enhance scaffold-cell interactions, facilitate neural electrical stimulation, guide axon formation, and promote neural differentiation.[14–16] Graphene is a two-dimensional carbon nanomaterial with a hexagonal honeycomb lattice composed of carbon atoms and sp^2 hybridized orbitals.[17,18] The double-bonded structure of graphene allows it to attach to specific functional groups or molecules through addition reactions.[19] However, graphene oxide (GO), a derivative of graphene, offers superior hydrophilicity due to its oxygen-containing functional groups, making it more suitable for clinical applications.[20] GO promotes stem cell adhesion, proliferation, and differentiation and can serve as a biosensor and drug carrier.[21] The hydrophilic nature of GO enhances cellular adhesion and migration, while its ability to interact with bioactive molecules makes it an ideal candidate for SCI treatment.[22]

In this study, we designed an electrospun scaffold incorporating GO and anti-TNF-α to achieve comprehensive SCI treatment. The anti-TNF-α component aims to suppress early inflammatory responses and establish a conducive immune microenvironment for regeneration. Meanwhile, GO serves as a structural and biochemical platform to support long-term neural differentiation and axonal growth. By integrating these properties, we propose a biomaterial that offers a multi-phase, multi-functional strategy for SCI repair, addressing both acute inflammatory damage and subsequent neuroregeneration.

Materials and Methods

Preparation of Electrospun Materials

For electrospinning solution preparation, the solvent 1,1,1,3,3,3-hexafluoro-2-propanol (hexafluoroisopropanol) was purchased from Aladdin (#H107504-500g; Shanghai, China). PLA was obtained from Jinan Daigang Biomaterial Co., Ltd. (Jinan, China), GO from Nanjing JCNANO Technology Co., Ltd. (#JCGO-98-1-75; Nanjing, China), and anti-TNF -α from Cloud-Clone Corp. (formerly USCN Life Science Inc.). The PLA+GO+Ab composite was prepared by dissolving 9% PLA, 0.5% GO, and 0.1% anti-TNF-α (1 mg/mL) in hexafluoroisopropanol (HFIP), followed by continuous stirring at room temperature (23–27°C) to ensure uniform dispersion. The electrospinning solution was then processed to generate nanofibrous scaffolds. Electrospinning was performed under optimized conditions with a voltage range of 13–16 kV, temperature 30–34°C, and relative humidity 60–68%. The flow rate was set at 0.5–1 mL/h to ensure uniform fiber formation.

Characterization of the Material

The surface morphology of the nanofibers was observed using scanning electron microscopy (SEM, TM3030, Hitachi, Japan). Elemental distribution analysis was performed using energy dispersive X-ray spectroscopy (EDS) mapping, detecting the C and O peaks to evaluate the material composition. Structural analysis of the materials was conducted using Fourier-transform infrared spectroscopy (FTIR, Nicolet iS50, Thermo Fisher Scientific, USA). Compositional analysis was performed using tip-enhanced laser confocal Raman spectroscopy (inVia-Reflex, Renishaw, UK). To further confirm the functionalization of GO, X-ray photoelectron spectroscopy (XPS, ESCALAB 250Xi, Thermo Fisher Scientific, USA) was performed. Crystalline structure analysis was carried out using X-ray diffraction (XRD, Rigaku SmartLab SE, Japan). Surface charge analysis was conducted using a solid surface zeta potential analyzer (SurPASS 3, Anton Paar, Austria). Surface topography and nanostructure was examined using atomic force microscopy (AFM, Dimension Icon, Bruker, Germany).

Culture of RAW264.7 Cells

The murine leukemia monocyte/macrophage cell line RAW264.7 was purchased from the Cell Bank of the Chinese Academy of Sciences (catalog no. SCSP-5036). The cells were cultured in DMEM supplemented with 10% fetal bovine serum (Sigma-Aldrich, catalog no. F8687), 1% penicillin/streptomycin (Beyotime, catalog no. C0222), and 1% L-glutamine (Beyotime, catalog no. C0212) and maintained at 37°C and 5% CO_2. The cells were passaged when confluence reached 90%.

RAW264.7 cells were treated with IFN-γ (20 ng/mL) and LPS (1 µg/mL) for 24 h to establish an LPS stimulation model. Cells from the LPS stimulation group were cultured with the relevant materials for 48 h before collection for subsequent analyses. Each experiment was independently conducted in triplicate.

Establishment of the Spinal Cord Injury Model

All procedures were performed following the National Institutes of Health Guidelines for the Care and Use of Laboratory Animals (1996). The experiments were approved by the Animal Care and Use Committee of The First Hospital Affiliated to Harbin Medical University (No. 2020052). SD rats were provided by the Experimental Center of Harbin Medical University.

The SD rats (250–300 g) were divided into the SCI, SHAM, PLA, PLA+GO, PLA+Ab, and PLA+GO+Ab groups (n=8 per group). The rats were anesthetized with sodium pentobarbital (30 mg/kg). A longitudinal incision was made along the midline of the back to expose the spine. Dorsal laminectomy was performed at T10 using fine rongeurs, and the spinal cord tissue was transected using fine microsurgical scissors. An electrospun piece of the composite material was placed on the transection injury area. Hemostasis was achieved using cotton swabs, the soft tissues were sutured, and the skin was sutured layer by layer. After 8 weeks, the rats were sacrificed via neck dislocation, and their spinal cord tissues were collected for follow-up experiments. The spinal cord, with a total length of about 50 mm, was excised for subsequent experiments. Throughout the experiment, no significant signs of systemic toxicity were observed in any of the experimental animals, including body weight loss or abnormal behavior. HE staining of major organs (lung, heart, liver, spleen, and kidney) revealed no evident histopathological changes, further confirming the biocompatibility and non-toxicity of the composite materials (Figure S3).

Cell Proliferation Assay

As above, the C17.2 cells (CC-Y2130, Shanghai EK-Bioscience Biotechnology Co., Ltd, China) were cultured at 37°C and 5% CO_2. Their proliferation capability was assessed using the CCK-8 assay. Approximately 5×10^3 cells were seeded into each well of a 96-well plate and incubated overnight. The medium containing the composite materials was added to the wells and incubated for 72 h. The CCK-8 solution (MA0218; Meilunbio, China) was added, and the cells were incubated for another 4 h. The optical density was measured at 450 nm using a microplate reader (Multiskan FC, Thermo Fisher Scientific). Relative cell viability was calculated based on the percentage of live cells in the total cell population.

Cell Scratch Assay

Cells from each group were seeded into a 6-well plate and cultured until reaching 100% confluence. A sterile pipette tip was then used to create a linear scratch across the monolayer of cells. The scratch areas were observed and photographed under a microscope at 0 hours and 72 hours post-scratch. Image analysis software was used to quantify the scratch area, and the scratch healing rate was calculated using the formula:

$$Scratch\ healing\ rate = \frac{Scratch\ area\ at\ 0\mathrm{h} - Scratch\ area\ at\ 72\mathrm{h}}{Scratch\ area\ at\ 0\mathrm{h}} \times 100\%$$

The experiment was repeated three times, and the average scratch healing rate was reported.

Cell Migration Assay

After co-culturing for 72 hours, cells from each group were harvested, digested, and counted. The cells were then resuspended in serum-free medium at a predetermined dilution and seeded uniformly into the upper chamber of a Transwell insert. The lower chamber contained culture medium supplemented with 10% fetal bovine serum (FBS). After 24 hours of incubation, the Transwell insert was removed, and a cotton swab was used to carefully remove the non-migrated cells from the upper chamber. The remaining cells on the bottom side of the insert were washed three times with phosphate-buffered saline (PBS), followed by fixation with 4% paraformaldehyde (143174, Biosharp, China) for 10 minutes at room temperature. The fixed cells were washed three times with PBS, stained with crystal violet (C0121, Beyotime, China) for 30 minutes at room temperature, and then washed again with PBS. The cells were observed under a microscope, photographed, and the number of migrated cells was quantified using image analysis software.

Immunofluorescence Assays to Identify Neuronal Cells

C17.2 cells were cultured as described above. The respective materials were added to each group, and the cells were co-cultured for 3 d. Following this period, immunofluorescence staining was performed for identification. After 3 d of induction, the culture medium was discarded, and the cells were washed three times with phosphate-buffered saline (PBS), each wash lasting 5 min. Cells were then fixed with 4% paraformaldehyde (143174, Biosharp, China) at room temperature for 10 min. Post-fixation, cells were washed three times with PBS, each wash lasting 5 min. Blocking was performed using 2% BSA (MB4219, Meilunbio) for 30 min. After removing the BSA, the primary antibodies DCX (1:100, A14611, ABclonal, China) and βIII-Tubulin (1:100, A18132, ABclonal, China) were added, and the cells were incubated overnight at 4°C. The next day, after returning to room temperature, the cells were washed three times with PBS, each for 5 min. Goat anti-Mouse IgG (H+L) Highly Cross-Adsorbed Secondary Antibody, Alexa Fluor™ 594 (1:1000, A-11032, Thermo, USA) and Goat anti-Rabbit IgG (H+L) Highly Cross-Adsorbed Secondary Antibody, Alexa Fluor™ 488 (1:1000, A-11034, Thermo, USA) were added, and the cells were incubated at 37°C for 1.5 h, wrapped in aluminum foil. Post-incubation, the cells were washed three times with PBS, each for 5 min. DAPI staining solution (10 µg/mL; MA0128, Meilunbio) was added and the cells were incubated in the dark for 10 min, followed by three PBS washes, each for 5 min. An anti-fade mounting medium (MA0221, Meilunbio) was added, and the cells were immediately observed and photographed under a fluorescence microscope.

Gene Silencing Experiment

To silence the expression of FGF1 protein, siRNA was applied (purchased from Seven Biotech, Beijing). One day prior to transfection, 5×10^5 cells were seeded into each well of a 6-well plate with 2 mL of culture medium per well. When cell confluence reached 40%-50%, transfection was performed. According to the transfection reagent protocol, 60 pmol of siRNA was diluted in 125 μL of Opti-MEM (Procell, catalog no. SF1001), and 3 μL of Lipofectamine 2000 (Thermo Fisher, catalog no. 11668027) was diluted in 125 μL of Opti-MEM to prepare the transfection reagent. The two solutions were mixed gently and allowed to sit at room temperature (20–25°C) for 10–20 minutes to form the transfection complex. The siRNA-transfection reagent complex was then gently added to the C17.2 cell culture wells, and the plate was gently shaken to ensure uniform distribution. A total of 0.74 mL of serum-free Opti-MEM was added to each well, and after 4–6 hours of incubation in the cell culture incubator, the medium was replaced with complete medium. After 48 hours, qPCR was performed to evaluate the silencing efficiency.

Western Blotting

Total cell lysates were prepared using cell lysis buffer (Beyotime, catalog no. P0013B) and subjected to denaturation by boiling. The total protein concentration was quantified using a BCA Protein Assay Kit (Solarbio, PC0020). Equal amounts of protein were mixed with 5× sample buffer, separated using sodium dodecyl sulfate-polyacrylamide gel electrophoresis (6% gel for NG2, PDGFRα, CD206, p-PI3K and PI3K; 8% for CD86, p-AKT and AKT; 10% for A2B5 and TGF-β3; 15% for FGF1), and transferred onto nitrocellulose membranes (Beyotime, catalog no. FFP26). The membranes were incubated overnight at 4°C with primary antibodies against A2B5 (1:1000, Invitrogen, catalog no. 2295008), PDGFRa (1:1000, ABclonal, catalog no. A2103), NG2 (1:1000, Abcam, catalog no. ab275024), TGF-β3 (1:200, ABclonal, catalog no. A17913), CD86 (1:500, ABclonal, catalog no. A16805), CD206 (1:700, Abcam, catalog no. ab300621), FGF1 (1:1000, ABclonal, catalog no. A5900), PI3K (1:1000, ABclonal, catalog no. A4992), p-PI3K (1:1000, ABclonal, catalog no. AP4027), AKT (1:1000, CST, catalog no. 2938T), p-AKT (1:1000, CST, catalog no. 4051S). The membranes were then treated with a 1:1000 dilution of a goat anti-rabbit secondary antibody (Thermo Fisher Scientific, catalog no. 31460). Signals were detected using an automatic luminescence imaging system (Tanon, Tanon-5200).

qPCR Analysis

Total RNA was extracted from the spinal cord of SD rats and raw 264.7 cells and C17.2 cells using an RNA Extraction Kit (Beyotime, R0017M). RNA was reverse-transcribed into first-strand cDNA using a BeyoRT II cDNA First Strand Synthesis Kit (Beyotime, D7168S). qPCR was performed using BeyoFast SYBR Green qPCR Mix (Beyotime, D7260) on an ABI ViiA7 Real-Time PCR System (Applied Biosystems). Each sample was analyzed in triplicate under the following reaction conditions: (a) pre-denaturation at 95°C for 2 min, (b) denaturation at 95°C for 15 s, (c) annealing/extension at 60°C for 15–30s, (d) steps (b) and (c) were repeated for a total of 40 cycles, and (e) optional melting curve analysis: 95°C for 15 s, 60°C for 15 s, and 95°C for 15 s. The primers were designed using Primer Premier 5.0 (San Francisco, CA, USA) (Table 1 and 2). All primers were synthesized by Sangon Biotech Co. Ltd. (Shanghai, China). Relative gene expression was normalized to GAPDH and β-Actin mRNA levels and calculated using the $2^{-\Delta\Delta Ct}$ method.

Flow Cytometry Analysis

RAW264.7 cells were collected by centrifugation at 1696 × g for 3 min, the supernatant was discarded, and the cells were washed with PBS before being transferred to new 1.5-mL centrifuge tubes. Each tube received 100 μL of 1× PBS and was centrifuged at 4°C and 1000 rpm for 3 min, after which the supernatant was discarded. Cells were resuspended in 100 μL of 1× PBS, and CD86 (Biolegend, 105005) and CD206 antibodies (dilution of 2 μL per 100 μL; Biolegend, 141719) were added for incubation on ice. The cells were washed twice with 1× PBS, resuspended in 500 μL 1× PBS, gently mixed, and analyzed using flow cytometry within 1 h using an FACS Calibur flow cytometer (NovoCyte 3110; Agilent, USA). In Vivo Flow Cytometry: Spinal cord tissues were enzymatically digested to obtain single-cell suspensions, followed by centrifugation at 1500 rpm for 6 minutes. The supernatant was discarded, and the cells were resuspended in HBSS. To block non-specific binding, Fc blocking reagent (CD16/CD32 Monoclonal Antibody, Invitrogen, catalog no. 14-0161-81) 1μL was added to the

Table 1 Primer Sequences

Gene	Primer Sequence (5′→3′)
Gapdh-Rat-F	TCTCTGCTCCTCCCTGTTCTA
Gapdh-Rat-R	GGTAACCAGGCGTCCGATAC
Map2-Rat-F	GCTGCTGGAAGAGTCAAAGA
Map2-Rat-R	CTGTCTTGGTCAAACTCCCTAC
Rgma-Rat-F	CGTGCAGGTCACCAATACA
Rgma-Rat-R	CTTTCTGGTCCACACACTCTT
β-Actin-Mus-F	CACTGTCGAGTCGCGTCC
β-Actin-Mus-R	TCATCCATGGCGAACTGGTG
CD86-Mus-F	GGGACCGTTCTCTACAAAA
CD86-Mus-R	TTGGGCTGAGATGACATGA
CD206-Mus-F	GCTGTGTGCAGAGGAGAAAG
CD206-Mus-R	CCACTGCTGTTGGTGATGTA
Fgf1-Mus-F	GGGGAGATCACAACCTTCGC
Fgf1-Mus-R	GTCCCTTGTCCCATCCACG

Table 2 Si-RNA Sequence

siRNA	Primer Sequence (5′→3′)
siFgf1-Mus-F	UACAAAUGAAUCUGAAUACAG
siFgf1-Mus-R	GUAUUCAGAUUCAUUUGUAUG

cell suspension and incubated on ice for 5 to 10 minutes. After blocking, a Live/Dead staining dye (1:1000, Invitrogen, catalog no. L34955) was added and incubated on ice for 30 minutes. The stained cells were then washed twice with HBSS, centrifuged at 300 g for 5 minutes each time, and resuspended in HBSS. For macrophage selection, CD68 antibody (2:100, Biolegend, catalog no. 137006) was added to the cell suspension at a ratio of 0.3 μL per 100 μL of sample and incubated at 4°C for 30 to 60 minutes in the dark. The cells were then washed, and fixation/permeabilization buffer (100 μL) was added. The suspension was gently mixed and incubated in the dark for 45 to 60 minutes. For intracellular staining, CD86 and CD206 antibodies were added at a dilution ratio of 2 μL per 100 μL of sample. The samples were incubated at 4°C for 30 to 60 minutes in the dark. After incubation, the cells were washed twice with HBSS, centrifuged at 300 g for 5 minutes each time, and resuspended in HBSS before filtering. The processed cells were analyzed using a FACS Calibur flow cytometer. Isotype-matched controls were used for statistical analysis, with a threshold of ≤1% positive cells in the negative control to ensure specificity.

In vitro Antibody Release Assays

RAW264.7 cells were divided into the control group (no treatments), LPS+IFNγ group, PLA group, PLA+GO group, PLA+Ab group, and PLA+GO+Ab group. The cell supernatant was collected at 0, 8, 16, 24, 48, and 72 h. The collected cell supernatant was centrifuged at 300 × g and 4°C for 10 min, and the supernatant was retrieved for detection. Cytokine detection was performed in accordance with the ELISA instructions (mlbio). The captured antibodies were incubated in 96-well plates at 4°C overnight. Nonspecific antigens were blocked with assay diluents. The standard and samples were added and incubated at 37°C for 2 h. After thoroughly washing with 0.05% Tween-PBS, the plates were incubated with detection antibodies for 1 h and HRP for 30 min. Finally, the color was developed with TMB, and the value of optical density was detected with a microplate spectrophotometer (Thermo). Mouse TNF-α kit (YJ002095) was purchased from Shanghai Enzyme Link Biotechnology Co., Ltd. (Shanghai, China).

Assessment of Motor Recovery

The BBB locomotor rating scale was used to assess hindlimb functional recovery.[23] The BBB is a 21-point scale that evaluates hind limb motor recovery after spinal cord injury. The BBB score quantifies motor function recovery in rats after spinal cord injury, with scores ranging from 0 (complete lack of motor function) to 21 (normal motor function) (Table S1). Owing to the hemisection injury, the right hindlimb (ipsilateral) and left hindlimb (contralateral) were assessed separately by two examiners. The animals were assigned new identification codes postoperatively to ensure a blind assessment of behavioral performance.

Hematoxylin and Eosin (HE) Staining

For paraffin section preparation, the paraffin blocks were cooled on ice for 2 hours. The tissue was then sectioned into 4-μm-thick slices using a microtome. The sections were dewaxed with xylene and rehydrated by passing through decreasing concentrations of ethanol (absolute ethanol to 75% ethanol), followed by incubation in distilled water for 5 minutes. For staining, the slides were first stained with hematoxylin for 10 minutes, rinsed with distilled water, and then stained with eosin for 2 minutes. After staining, the slides underwent dehydration and clearing through graded ethanol solutions and xylene. Finally, the sections were mounted with neutral resin, ensuring air bubbles were removed, and then observed under a light microscope.

Histological Immunofluorescence

Tissues were fixed in 4% paraformaldehyde for 24 h, dehydrated, paraffin-embedded, and cut into 4-μm-thick sections. The primary antibodies against Nestin (1:200, Abclonal, catalog no. A11861), PDGFRa (1:1000, Abcam, catalog no. ab203491), NG2 (1:1000, Abcam, catalog no. ab275024), A2B5 (1:1000, Invitrogen, catalog no. 2295008), TGF-β3 (1:200, ABclonal, catalog no. A17913), and GAP43 (1:1000, ABclonal, catalog no. A19055) were added and incubated at 4°C overnight. The following day, the sections were warmed for 1 h, washed with PBS three times for 5 min each, and then incubated with secondary antibodies (1:200) at 37°C for 1 h. After washing with PBS, the sections were incubated with DAPI (Biosharp, catalog no. BS097) for 10 min, mounted with an anti-fade mounting medium (MA0221; Meilunbio), and observed and photographed under a conventional light microscope (Olympus, BX53).

Statistical Analysis

All data were analyzed using GraphPad Prism 9.0 software (GraphPad Software, La Jolla, CA, USA) and presented as means ± standard deviation. Multiple-group comparisons were performed using one-way analysis of variance, with Tukey's significant difference post-hoc test. Significance was defined as $P<0.05$.

Results

Composite Material Characterization

The microstructure of PLA and PLA+GO electrospun nanofibers was observed using scanning electron microscopy (SEM), which showed that the electrospinning of PLA generated uniform, smooth, and randomly oriented nanofibers (Figure 1A and B). The addition of GO caused no significant change to the microstructure of the PLA fibers. Use Energy Dispersive Spectroscopy (EDS) Mapping were used to examine the morphology and elemental distribution of the composite materials. In contrast, the corresponding EDS Mapping results of PLA+GO reveal a significant increase in C element (red color) after GO incorporation.

In the Fourier-transform infrared spectroscopy spectra, the weak absorption peaks at 2994 and 2940 cm^{-1} were attributed to the C-H stretching vibrations of PLA. The relatively strong absorption peak at 1747 cm^{-1} corresponded to the stretching vibration of C=O. The absorption peak at 1456 cm^{-1} corresponded to the bending peak of -CH_3. The 1385 and 1357 cm^{-1} peaks were attributed to the deformation of C-H, including symmetric and asymmetric bending peaks. The absorption peaks at 1179, 1128, and 1084 cm^{-1} were due to C-O stretching vibrations, and the weak absorption peak at 1047 cm^{-1} was attributed to the bending peak of -OH (Figure 1C).

The Raman spectra (Figure 1D) primarily consisted of G and D peaks. The G peak, which appeared around 1580 cm^{-1}, is the main characteristic peak indicating the graphitization of carbon materials and is formed by the vibrations of aromatic rings. The D peak is generally considered the absorption vibration peak of carbon defects and disordered carbon. In the PLA samples, weaker absorption peaks near 931, 1415, and 1741 cm^{-1} were associated with the

https://doi.org/10.2147/IJN.S509954

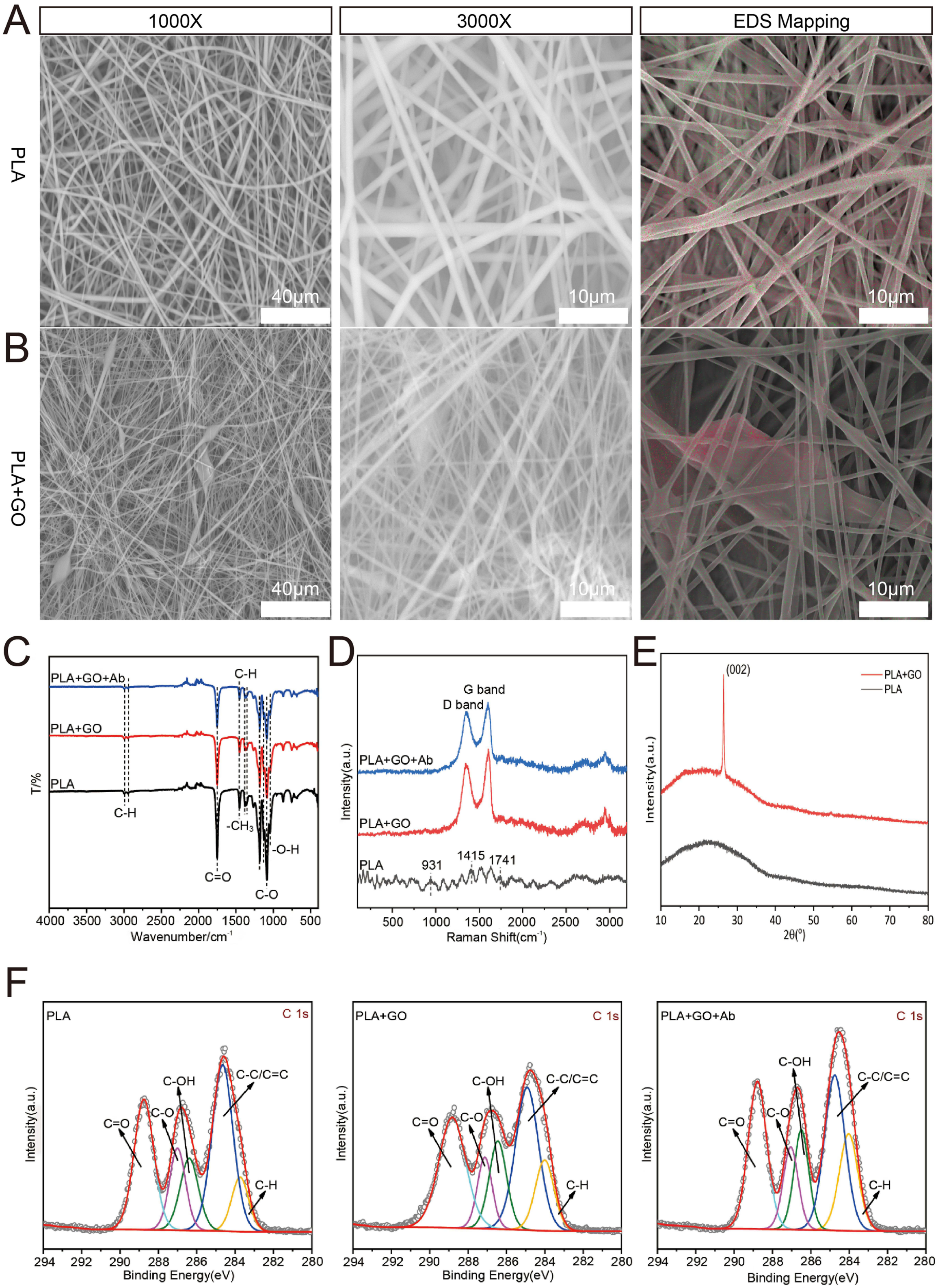

Figure 1 Characterization of the scaffold. (**A** and **B**) Scanning electron microscopy (SEM) morphology and Energy Dispersive Spectroscopy (EDS) Mapping of PLA and PLA +GO; top: 1000×, bottom: 3000×. (**C**) Fourier-transform infrared spectroscopy (FTIR) spectra of PLA, PLA+GO, and PLA+GO+Ab. (**D**) Raman spectra of PLA, PLA+GO, and PLA+GO+Ab. (**E**) X-ray diffraction (XRD) patterns of PLA and PLA+GO. (**F**) X-ray photoelectron spectroscopy (XPS) spectra of PLA, PLA+GO, and PLA+GO+Ab.

stretching vibrations of C=O, asymmetric deformation vibrations of -CH3, and stretching vibrations of the C-COO repeating unit in the PLA materials, respectively. However, no significant D or G peaks were observed. In the PLA+GO samples, distinct D and G peaks were observed at 1355 and 1603 cm^{-1}, respectively. This indicated that GO was successfully incorporated into the PLA+GO composite.

X-ray diffraction (XRD) was performed to examine the crystallographic properties and dispersion of GO in the polymer matrix. Figure 1E displays the XRD patterns of PLA and PLA+GO composites. The XRD spectrum of pure PLA exhibits a broad scattering peak between $2\theta \approx 15°$ and 25°, which is characteristic of its amorphous structure. The absence of sharp diffraction peaks indicates the lack of long-range order in PLA. In contrast, the PLA+GO composite exhibits a new diffraction peak at $2\theta \approx 26.5°$, corresponding to the (002) plane of graphite. The sharpness and intensity of this peak indicate the high crystallinity of GO, suggesting that GO retains an ordered structure within the PLA matrix. The presence of this peak also implies that GO influences the molecular arrangement of PLA, potentially modifying its crystallization behavior.

X-ray photoelectron spectroscopy (XPS) showed that the peaks of PLA mainly corresponded to 283.9, 284.9, 286.4, 287.1, and 288.8 eV, representing C-H, C=C/C-C, C-OH, C-O, and C=O peaks, respectively. The PLA+GO spectra showed that, after functional modification, the area of the C=O peak of GO increased. This was probably because the hydroxyl groups on GO undergo esterification reactions with the carboxyl groups of lactic acid, transforming the carboxyl groups on GO into ester groups, thereby increasing the number of C=O groups (Figure 1F).

Zeta potential measurements (Figure S1) demonstrated that the incorporation of GO and anti-TNF-α altered the surface charge properties of the composite. At physiological pH (7.4), the PLA+GO+Ab material exhibited a more negative charge compared to PLA alone. Under acidic conditions (pH 6.0),[24] which mimic the inflammatory microenvironment of SCI, the Zeta potential of PLA+GO+Ab further decreased, which may enhance cellular adhesion and interaction.

The Atomic Force Microscopy (AFM) results (Figure S2) indicate that the incorporation of GO into PLA nanofibers increases surface roughness. The PLA+GO group exhibits a higher Rmax (maximum roughness), Ra (average roughness), and Rq (root mean square roughness) compared to pure PLA, suggesting that GO modification alters the fiber morphology, potentially enhancing surface interactions.

Promotion of Differentiation and Proliferation Effects of PLA+GO+Anti-TNF-α on Neural Stem Cells

Based on the cell counting kit (CCK)-8 cell proliferation assay (Figure 2A), the impact of GO and anti-TNF-α antibody on proliferative capacity was assessed in neural stem cells (NSCs) in control, PLA, PLA+GO, PLA–anti-TNF-α (PLA +Ab), and PLA–GO–anti-TNF-α (PLA+GO+Ab) groups. After 3 d, the PLA+GO and PLA+GO+Ab groups demonstrated higher cell viability than the PLA+Ab group, suggesting that GO promoted the proliferation of NSCs, whereas Ab alone had no effect. Compared with that in the control group, the differentiation of pro-NSCs into neural cells was higher in the PLA+GO ($P<0.0001$) and PLA+GO+Ab ($P<0.0001$) groups (Figure 2B and C).

Promotion of Migration Effects of PLA+GO+Anti-TNF-α on Neural Stem Cells

We conducted transwell (Figure 3A and C) and scratch assays (Figure 3B, D and E) to evaluate the effect of GO on NSCs migration. The transwell results demonstrated that the GO-treated groups (PLA+GO, PLA+GO+Ab) had significantly higher numbers of migrating cells compared to the control group ($p<0.0001$), indicating that GO effectively enhances NSCs migration. In the scratch assay, the GO-treated group exhibited a significantly smaller scratch area ($p<0.0001$) and a higher healing rate ($p<0.0001$) than the other groups, further confirming GO's role in promoting NSCs migration. Additionally, use Nestin as a marker for immunofluorescence analysis of spinal cord tissue at 7 and 14 days post-treatment showed that GO supplementation significantly enhanced NSCs migration (Figure 3F and G). At 7 days, the PLA+GO group displayed significantly higher Nestin expression compared to the SCI group ($p<0.01$), with an even greater effect observed in the PLA+GO+Ab group ($p<0.001$). In contrast, the group treated with Ab alone showed no significant enhancement, and no statistical difference was observed between the PLA+GO+Ab and PLA+Ab groups (ns). At 14 days, the PLA+GO group continued to exhibit a significant promoting effect compared to the SCI group ($p<0.001$). Notably, the PLA+GO+Ab group showed an even greater increase in Nestin expression at 14 days compared to 7 days

https://doi.org/10.2147/IJN.S509954

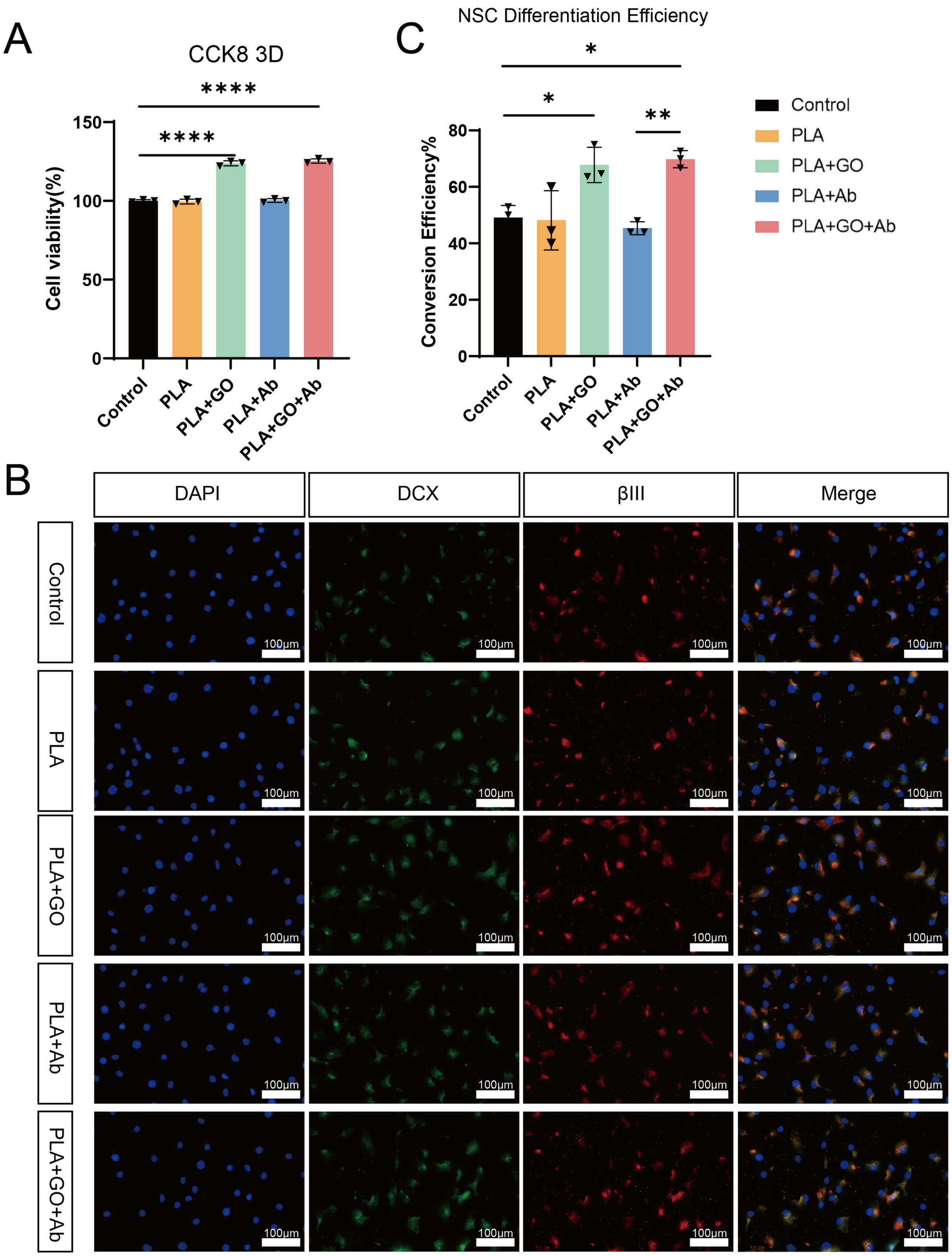

Figure 2 Effects of GO on Neural Stem Cell Proliferation and Differentiation. (**A**) CCK-8 assay. The addition of GO significantly promoted the proliferation of neural stem cells (NSCs) (n=3). (**B**) Differentiation of neural stem cells into neural cells. (**C**) NSC differentiation efficiency quantification, showing that PLA+GO+Ab significantly enhances neuronal differentiation efficiency compared to scaffolds without GO. (n=3) (*P<0.05, **P<0.01, ****P<0.0001).

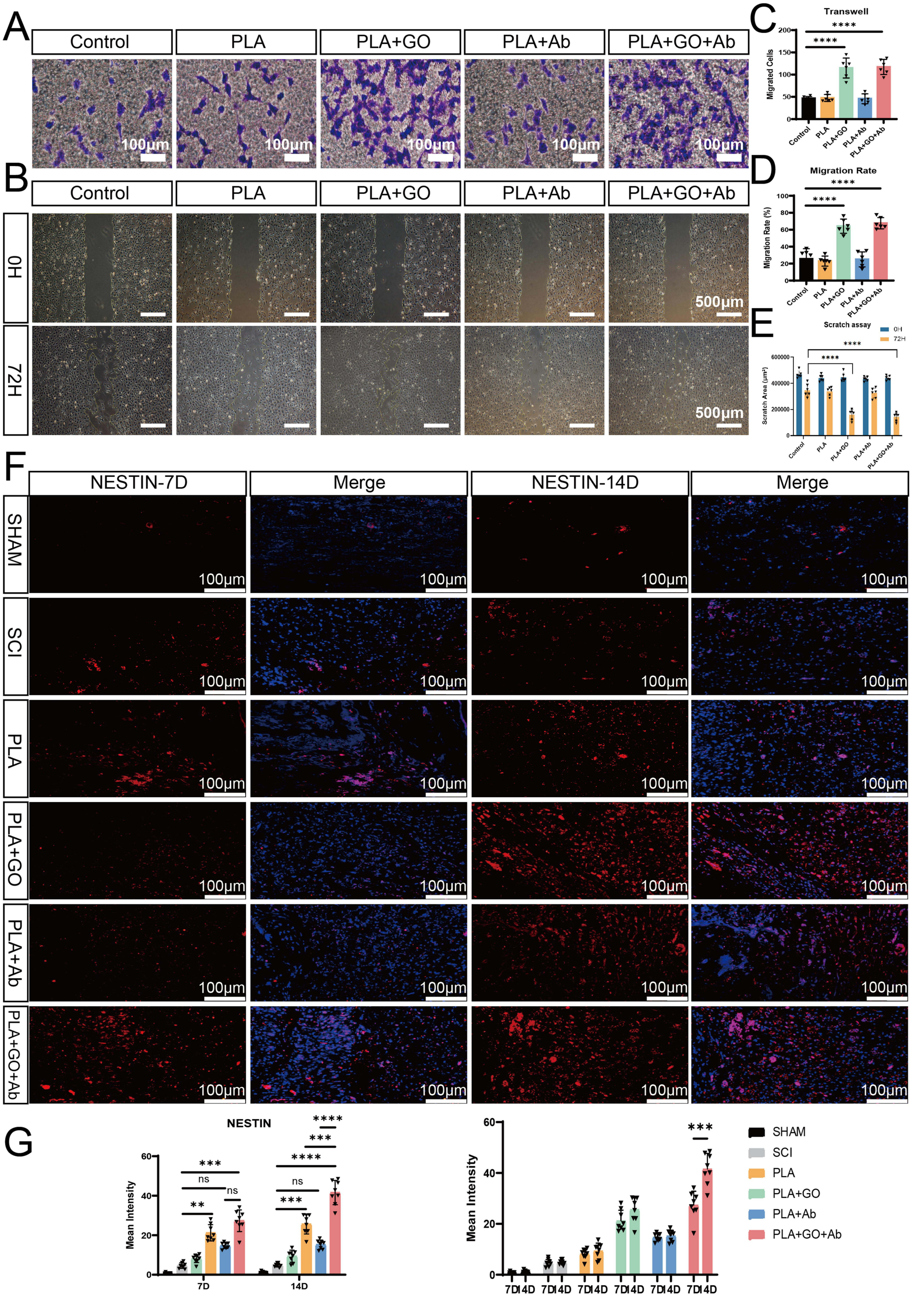

Figure 3 Effects of GO on Neural Stem Cell Migration. (**A** and **C**) Transwell assays demonstrate that the addition of GO significantly enhances neural stem cell migration. (n=6) (**B, D** and **E**) Scratch experiments showed that the addition of GO significantly promoted the healing of cell scratches by comparing the scratch areas at 0H and 72H. Statistical analysis of the scratch area and migration rate. (n=6) (**F** and **G**) Immunofluorescence staining of NESTIN in spinal cord tissue at 7 and 14 days shows that GO-treated groups (PLA+GO, PLA+GO+Ab) enhance the migration of neural stem cells, as indicated by increased NESTIN expression. However, by day 14, the PLA+GO group did not show a superior migration-promoting effect compared to the PLA+GO+Ab group. (n=8) (**P<0.01, ***P<0.001, ****P<0.0001).

Abbreviation: ns, not significant.

https://doi.org/10.2147/IJN.S509954

(p<0.001), with a significantly stronger effect than the PLA+Ab group (p<0.0001). No further significant effects were observed in the other groups over time.

GO Regulates Rap1 Signaling Pathway to Upregulate FGF1, Activating PI3K/AKT to Promote Neural Stem Cells Proliferation, Differentiation, and Migration

To further explore the mechanism by which GO regulates NSCs, RNA sequencing was performed on cells co-cultured with NSCs in the Control, PLA+Ab, and PLA+GO+Ab groups. GO intervention significantly altered gene expression in NSCs. Compared with the PLA+Ab group, the addition of GO resulted in substantial changes in gene expression, with 288 genes upregulated and 222 genes downregulated. The butterfly plot demonstrated that the observed gene expression changes induced by GO were statistically significant and not due to random noise (Figure 4A and B). Gene Ontology enrichment analysis revealed that these differentially expressed genes were primarily involved in processes such as neuron projection, extracellular matrix binding, lipid metabolism, and enzyme activity regulation, all of which are closely associated with NSC differentiation, migration, and morphological changes. Kyoto Encyclopedia of Genes and Genomes (KEGG) analysis indicated that these differentially expressed genes were associated with cell adhesion, polarity, and motility, highlighting several key biological pathways, including signal transduction (eg, Rap1 and PI3K-Akt pathways), extracellular matrix interactions, and actin cytoskeleton regulation. These pathways are likely to play crucial roles in the migration, differentiation, and metabolism of neural stem cells (Figure 4C and D). Figure 4E presents a Gene Set Enrichment Analysis (GSEA) plot for the RAP1 signaling pathway (MMU04015), comparing PLA+GO+Ab vs PLA+Ab

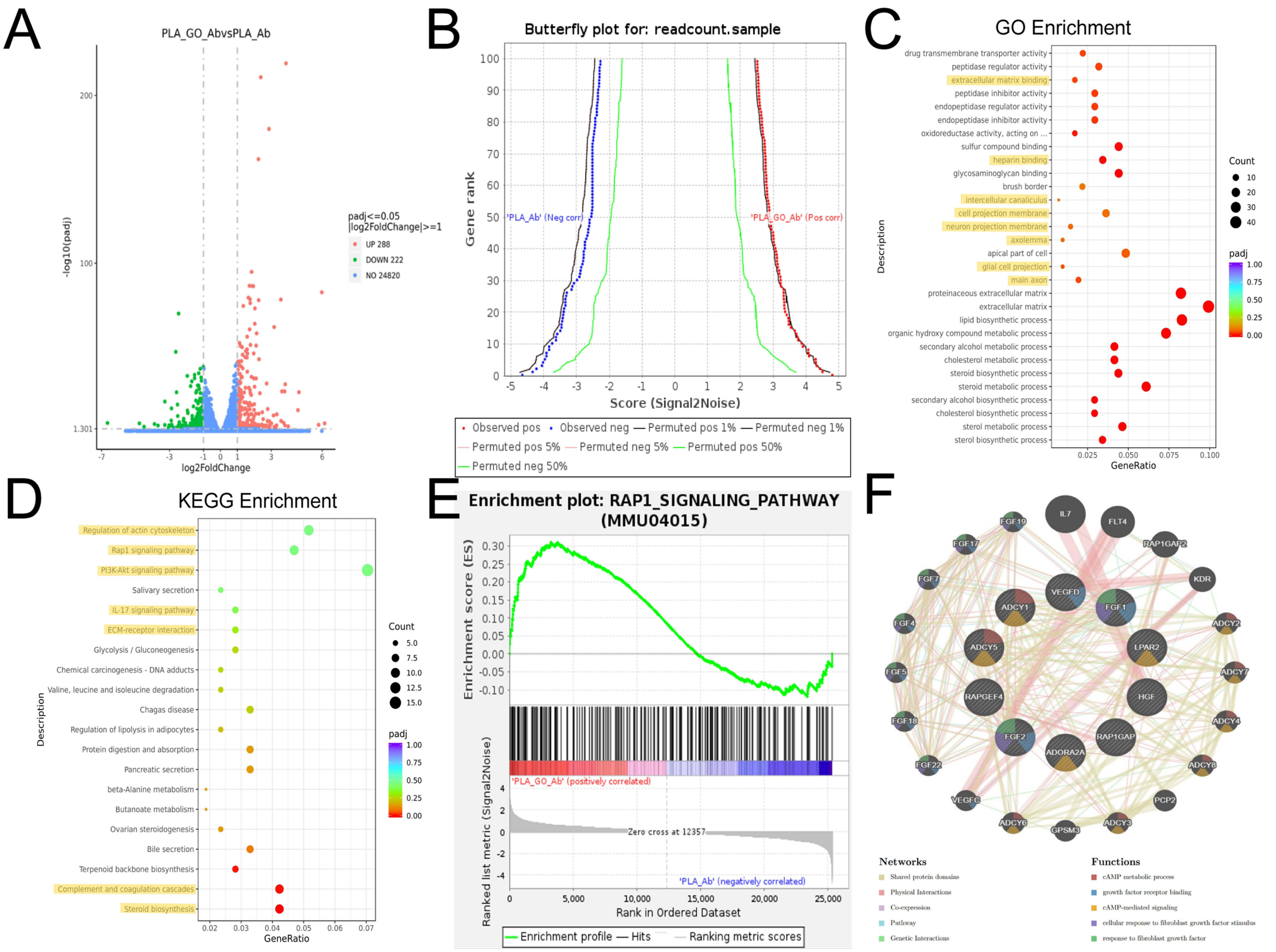

Figure 4 Continued.

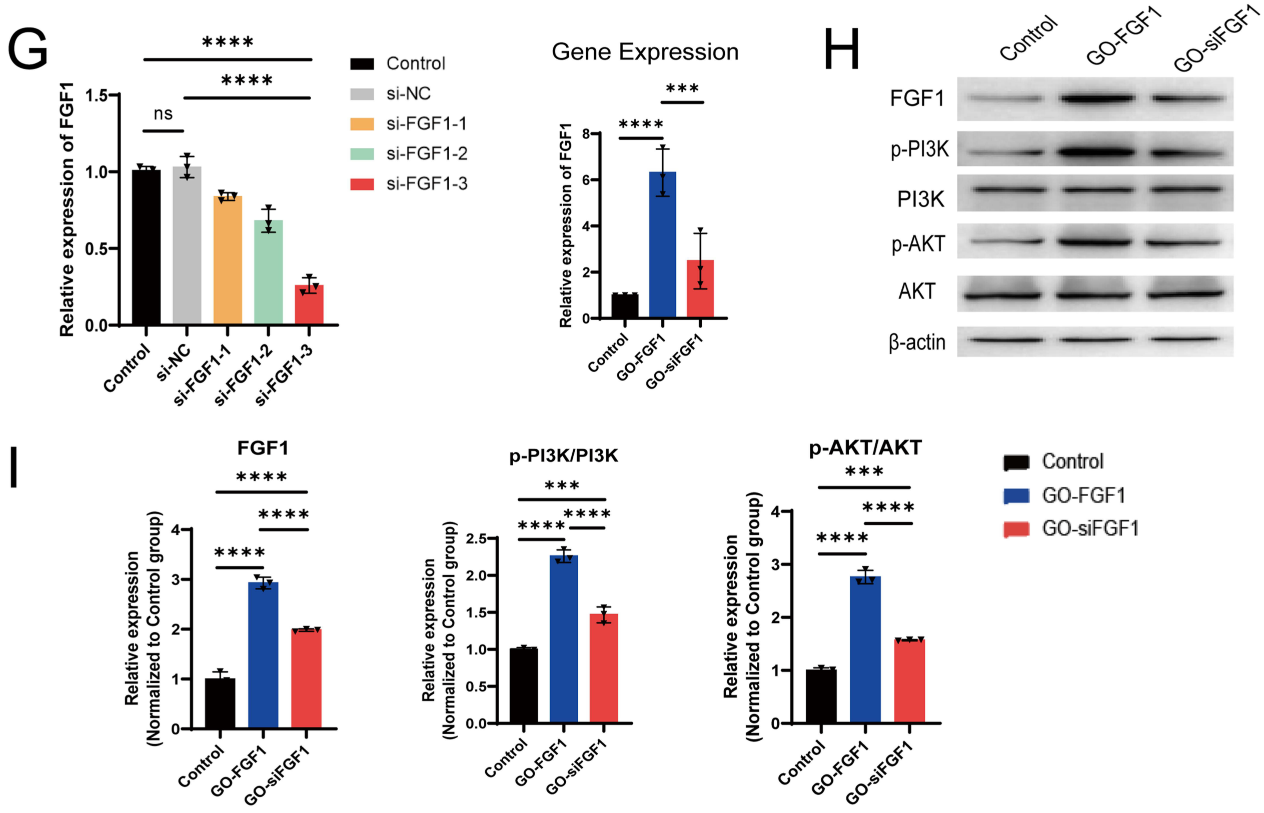

Figure 4 Sequencing Analysis and Validation of GO Effects on Neural Stem Cells. (**A**) A volcano plot illustrating differentially expressed genes between the PLA+Ab and PLA +GO+Ab groups. Green dots represent downregulated genes, while red dots indicate upregulated genes. (**B**) A butterfly plot depicting the signal-to-noise ratio for gene expression across the different experimental groups. The green and red lines highlight significant gene expression differences between the PLA+Ab and PLA+GO+Ab groups. (**C**) GO (Gene Ontology) enrichment analysis shown as a dot plot, with dot size representing the number of genes and color indicating statistical significance (adjusted p-value). This analysis underscores biological processes such as neural projection, extracellular matrix interactions, and lipid metabolism, which are critical for NSC function. (**D**) KEGG pathway enrichment analysis, highlighting the signaling pathways significantly affected by GO intervention. Key pathways such as Rap1, IL-17, and PI3K-Akt signaling, as well as ECM-receptor interaction, were enriched, revealing pathways involved in NSC adhesion, polarity, migration, and differentiation. (**E**) Gene Set Enrichment Analysis (GSEA) for the Rap1 signaling pathway, showing that genes involved in the Rap1 pathway are significantly upregulated in the PLA+GO+Ab group. (**F**) A protein-protein interaction (PPI) network, highlighting key proteins involved in the Rap1 signaling pathway and other related biological processes. The network shows interactions between proteins such as VEGFD, FGF1, and HGF, which are crucial for growth factor signaling, cAMP metabolism, and cell adhesion. (**G**) qPCR analysis of FGF1 expression following siRNA-mediated FGF1 silencing in NSCs. The bar graph demonstrates that FGF1 expression is significantly reduced in the GO-siFGF1 group compared to the Control and GO-FGF1 groups, confirming effective silencing. (n=3) (**H** and **I**) Western blot analysis of PI3K and AKT phosphorylation levels. The results indicate that PI3K and AKT phosphorylation is significantly elevated in the GO-FGF1 group compared to the Control group, while phosphorylation is reduced in the GO-siFGF1 group. Total PI3K and AKT protein levels remain unchanged across all groups, suggesting that GO specifically affects phosphorylation rather than total protein levels. (n=3) (***P<0.001, ****P<0.0001).

groups. The enrichment profile (green curve) represents the enrichment score, which quantifies the degree to which genes associated with the RAP1 signaling pathway are overrepresented at the top (positively correlated) or bottom (negatively correlated) of the ranked gene list. This result implies that GO enhances RAP1 signaling. Figure 4F illustrates the protein-protein interaction network of differentially expressed genes significantly altered in the Rap1 signaling pathway following GO regulation. These differentially expressed genes are involved in various biological processes, particularly cAMP metabolic processes and growth factor receptor binding.

To verify whether GO promotes NSC proliferation, differentiation, and migration through the Rap1 signaling pathway, we selected FGF1, a key protein in the Rap1 signaling pathway, for validation. We used siRNA to silence FGF1 expression and confirmed its knockdown efficiency, select si-FGF1-3 for subsequent experiments (Figure 4G). We then examined the phosphorylation levels of PI3K and AKT in the Control group, the PLA+GO+Ab group (GO-FGF1), and the FGF1-silenced group (GO-siFGF1). The results showed that PI3K and AKT phosphorylation levels were significantly elevated in the GO-FGF1 group, whereas they were markedly reduced in the GO-siFGF1 group compared to the GO-FGF1 group. Additionally, total PI3K and AKT protein levels in the GO-siFGF1 group showed no significant differences compared to the

Control group (Figure 4H and I). These findings indicate that GO upregulates FGF1, thereby activating the downstream PI3K/AKT signaling pathway, which promotes NSC proliferation, differentiation, and migration.

Promotion of the Polarization of M2 Phenotype Macrophages

We examined the effect of PLA+GO+Ab on macrophage polarization in RAW264.7 cells exposed to different conditions and materials to determine whether PLA+GO+Ab could modulate M1/M2 polarization. The expression of specific macrophage markers was assessed under different treatment conditions using Western blotting, qRT-PCR, ELISA, and flow cytometry. CD86 was used as an M1 macrophage marker, and CD206 as an M2 macrophage marker.

Western blot (Figure 5A) demonstrated that the PLA+GO+Ab group exhibited lower CD86 expression than the LPS+IFN-γ group ($P < 0.05$) and higher CD206 protein expression than the LPS+IFN-γ ($P < 0.01$) group. Meanwhile, compared with the LPS+IFN-γ ($P < 0.001$), PLA ($P < 0.001$), and PLA+GO ($P < 0.001$) groups, CD86 mRNA expression was the lowest in the PLA+GO+Ab group, whereas CD206 mRNA expression was the highest, suggesting that this scaffold promoted M2 macrophage polarization (Figure 5B and C).

ELISA (Figure 5D) showed that PLA+GO+Ab group exhibited significantly lower TNF-α levels compared to the LPS+IFN-γ group ($P < 0.0001$), indicating that the incorporation of anti-TNF-α effectively inhibited the release of inflammatory cytokines. Further analysis revealed that TNF-α levels in the PLA+Ab and PLA+GO+Ab groups gradually decreased from 8 hours onward and remained significantly reduced over 72 hours, suggesting a sustained and stable release of the antibody. It is important to note that this experiment detects the results of antigen-antibody binding reactions. The TNF-α antibody specifically binds to TNF-α at its corresponding epitope, forming antigen-antibody complexes, thereby neutralizing TNF-α activity. Since the ELISA kit specifically detects free TNF-α, the results showed a significant reduction in TNF-α levels. These findings indicate that the antibody effectively binds to the scaffold, providing a crucial theoretical basis for further research on inflammation regulation and therapeutic strategies.

Flow cytometry (Figure 5E) was used to compare CD86 and CD206 expression between groups. The LPS+IFN-γ group induced M1 macrophage polarization. In contrast, both PLA+Ab and PLA+GO+Ab groups significantly reduced CD86 expression and increased CD206 expression. Compared to the PLA+Ab group, the PLA+GO+Ab group exhibited a more pronounced reduction in CD86+ M1 macrophages and a significant increase in CD206+ M2 macrophages ($P < 0.0001$), confirming that these materials were more effective in promoting M2 macrophage polarization.

These findings suggest that the PLA+GO+Ab scaffold effectively suppresses M1 polarization, enhances M2 macrophage differentiation, and enables a sustained and stable release of antibodies, leading to effective inhibition of TNF-α activity. This provides a strong theoretical foundation for further studies on inflammation regulation and therapeutic applications.

Effects of Composite Scaffolds Enhances Motor Function Recovery and Neural Regeneration

In vivo experiments were performed to investigate whether PLA+GO+Ab scaffold could influence the outcomes of SCI. First of all, we assessed the effects of PLA+GO+Ab on motor function recovery and spinal cord tissue repair in rat models of SCI to evaluate the therapeutic potential of composite scaffold in SCI. The Basso–Beattie–Bresnahan (BBB) score graph illustrates the motor function recovery trends in six groups of rats following different treatments (Figure 6A). The PLA+GO+Ab group significantly enhanced motor function recovery, with a continuous improvement observed throughout the study period. From the 2nd week onward, the PLA+GO+Ab group showed a significant difference compared to the SCI group ($P < 0.01$). Additionally, by the 7th and 8th weeks, PLA+GO+Ab exhibited a statistically significant improvement over PLA+Ab ($P < 0.01$). Overall, the BBB scores suggest that the combination of GO with anti-TNF-α provides the most significant improvement in motor function recovery following SCI, highlighting the potential synergistic effect of these components.

Gross morphology of the spinal cord showed that the SHAM group maintained an intact spinal cord structure, whereas the SCI group exhibited severe damage. Notably, the PLA+Ab and PLA+GO+Ab groups displayed reduced spinal cord damage, with PLA+GO+Ab showing the most substantial structural recovery (Figure 6B). H&E staining and cavity area quantification (Figure 6C and D) demonstrated that the SCI group suffered extensive tissue damage and large

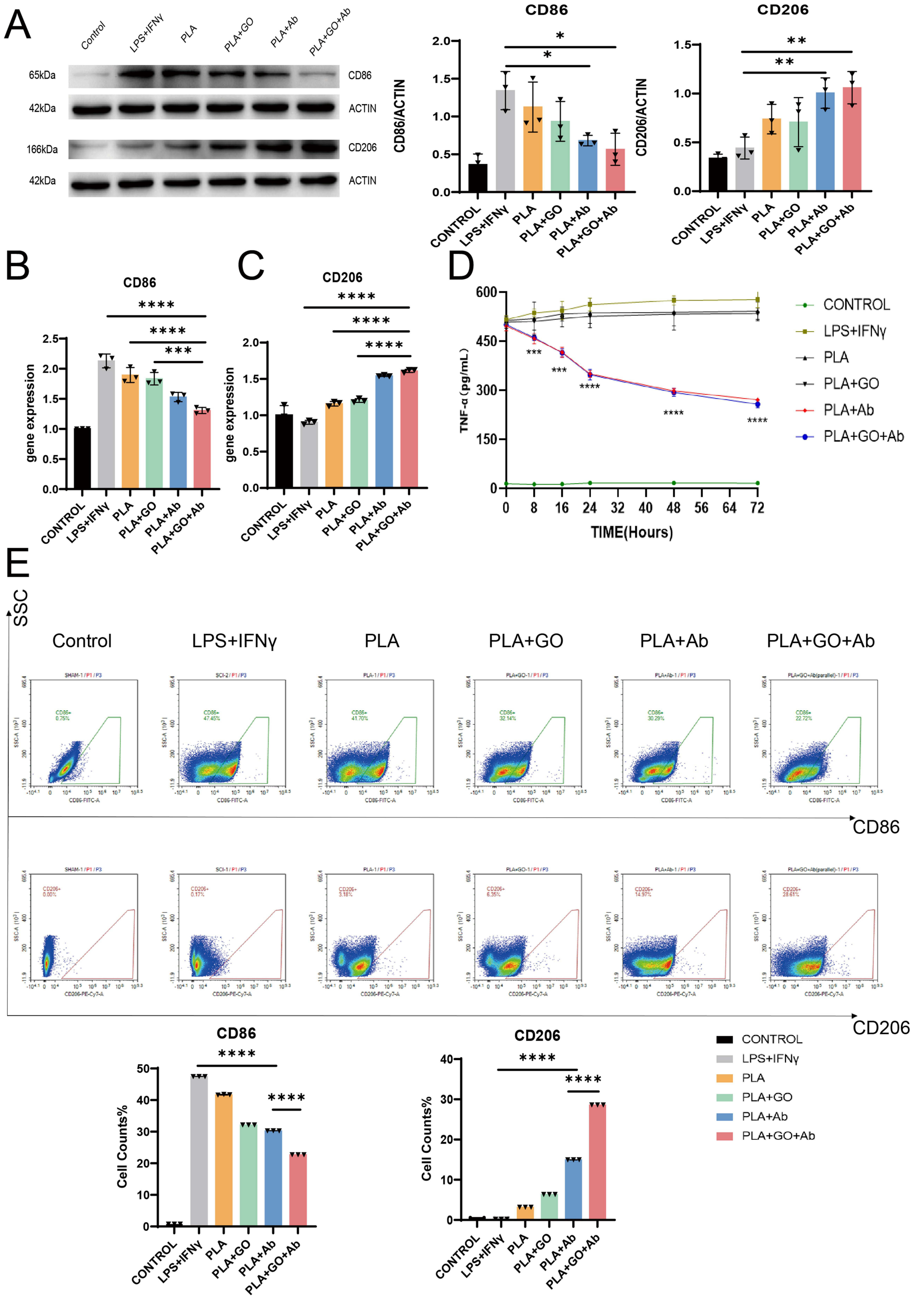

Figure 5 Effects of Composite Scaffolds on Macrophage Polarization and Inflammatory Response. (**A**) Western blot analysis of CD86 and CD206 protein expression in different groups. (n=3) (**B** and **C**) qRT-PCR quantification of CD86 and CD206 on mRNA levels. (n=3) (**D**) ELISA analysis of TNF-α levels in the culture medium over time. (**E**) Flow cytometry results showing the percentage of CD86 (M1) and CD206 (M2) macrophages. (n=3) (*P<0.05, **P<0.01, ***P<0.001, ****P<0.0001).

cavities, while PLA+GO and PLA+GO+Ab groups exhibited significantly reduced cavity areas compared to other groups ($P < 0.0001$). This further supports our in vitro findings, which demonstrated that GO promotes neural stem cell proliferation and migration, potentially contributing to enhanced spinal cord tissue repair.

Next, various proteins involved in neuronal regeneration were examined by immunofluorescence (Figure 6E and F). GAP43 is a crucial protein for axonal growth and regeneration following spinal cord injury,[25] GAP43 immunofluorescence and quantification showed that the PLA+Ab and PLA+GO+Ab groups exhibited significantly higher GAP43 expression, compared to other groups ($P < 0.0001$). Moreover, PLA+GO+Ab demonstrated a significant increase in GAP43 expression compared to PLA+Ab, suggesting that GO and Ab addition plays a synergistic crucial role in promoting axonal regeneration. qRT-PCR analysis of axonal regeneration-related mRNA expression further confirmed the regenerative potential of PLA+GO+Ab (Figure 6G). The expression levels of the RGMA and MAP2 genes, which are associated with axonal regeneration.[26] RGMA expression varied significantly among groups. The SCI model group exhibited a marked increase in RGMA expression. The PLA+GO+Ab group showed a significant decrease in RGMA expression compared with other groups ($P < 0.0001$). MAP2 expression was the highest in the sham group, indicating higher gene activity under physiological conditions. There was significantly increased in the PLA+GO+Ab group compared to SCI group and other groups ($P < 0.0001$).

Overall, these findings demonstrate that PLA+GO+Ab significantly enhances spinal cord repair, reduces cavity formation, and promotes axonal regeneration, highlighting its potential as an effective therapeutic strategy for SCI repair.

Regulation of Macrophage Phenotype by Composite Scaffolds in vivo

To explore how PLA+GO+Ab scaffold affects macrophage polarization, we examined the expression of macrophage markers CD86 (an M1 marker) and CD206 (an M2 marker) in spinal cord tissue. We first employed immunofluorescence to assess the expression of CD86 and CD206 within the tissue (Figure 7A and B). CD86+ macrophages were significantly increased in the SCI group, indicating a pro-inflammatory response. In contrast, CD206+ macrophages, associated with anti-inflammatory and tissue-repair functions, were markedly elevated in the PLA+GO+Ab group.

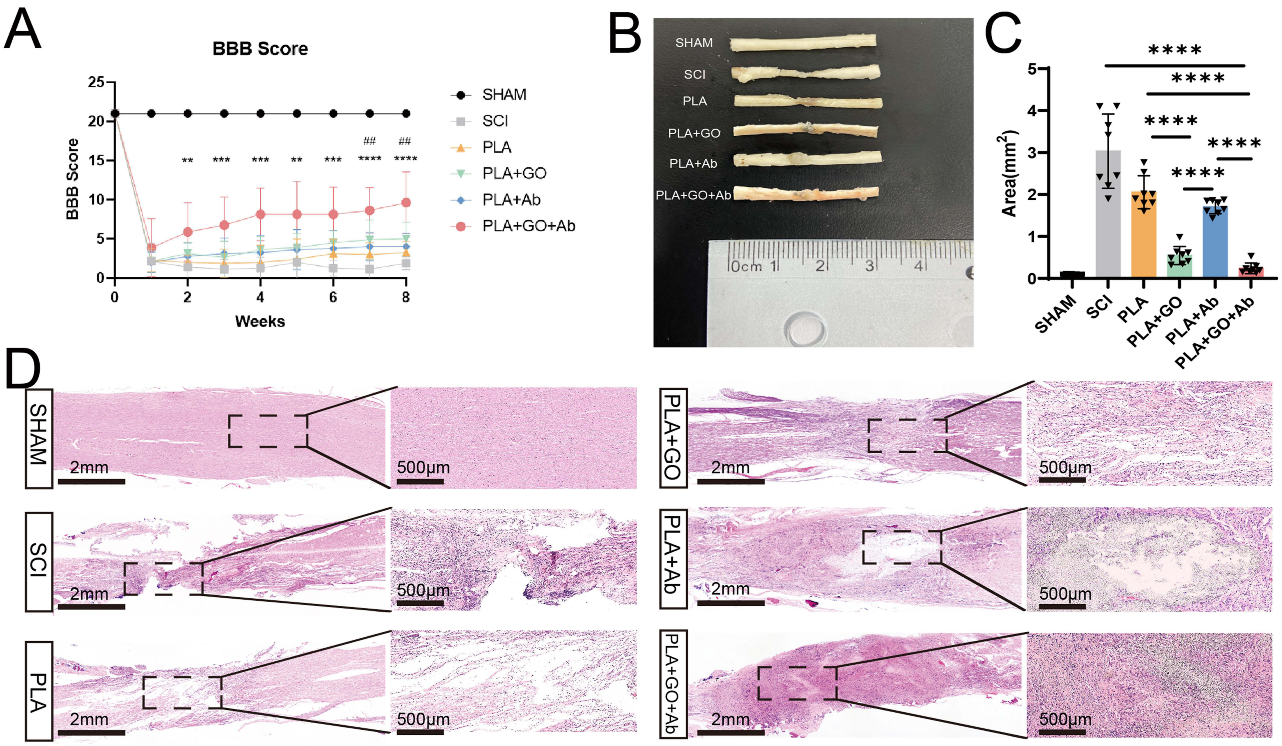

Figure 6 Continued.

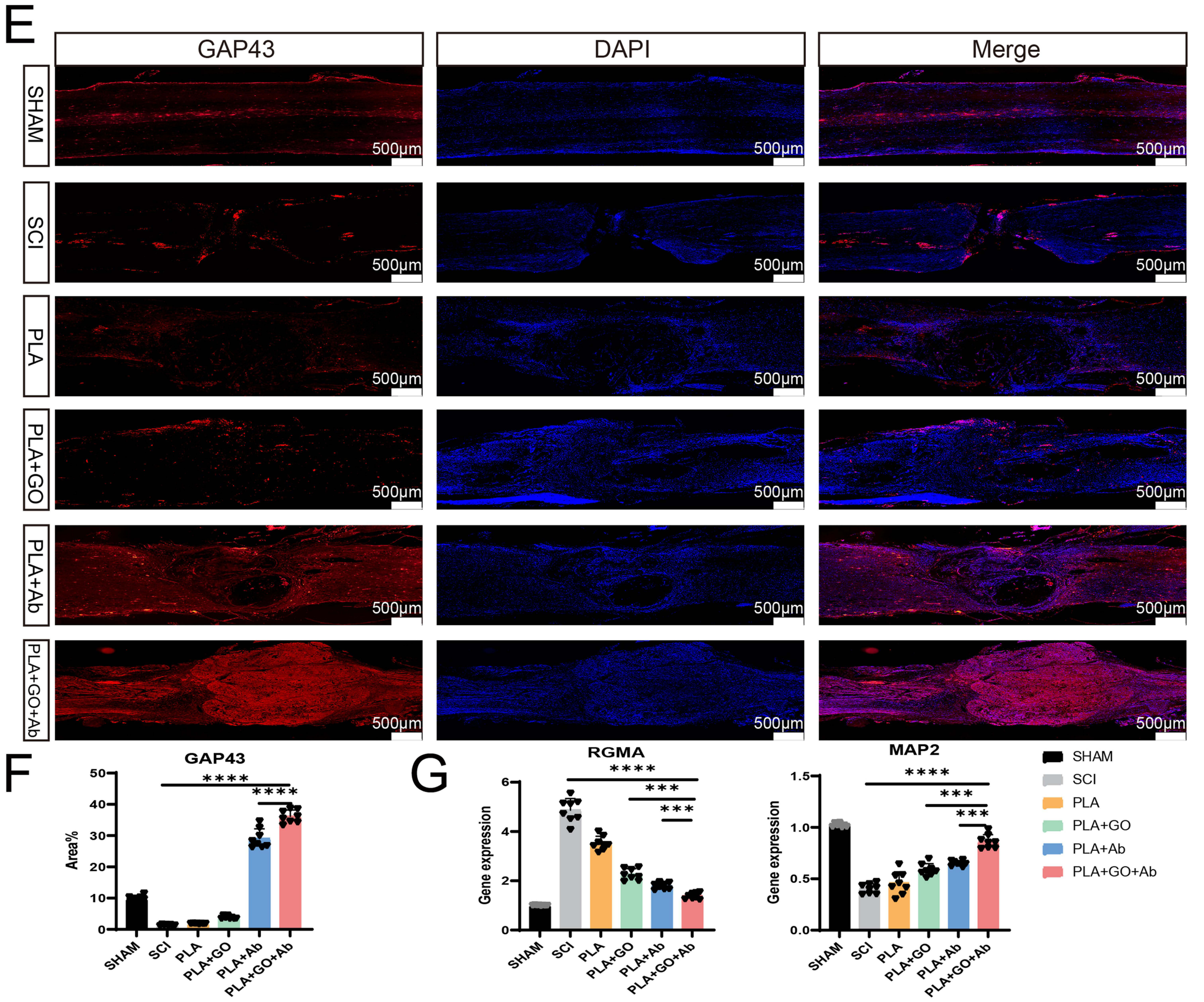

Figure 6 Effects of Composite Scaffolds on Spinal Cord Injury Repair and Neural Regeneration. (**A**) Basso–Beattie–Bresnahan (BBB) scores assessment over 8 weeks post-injury, showing motor function recovery in different groups. The PLA+GO+Ab group demonstrated significantly improved functional recovery. (n=8) (**P<0.01, ***P<0.001, ****P<0.0001 between the PLA+GO+Ab and SCI group. ##P<0.01, between the PLA+GO+Ab and PLA+Ab group). (**B**) Macroscopic observation of the spinal cord showed that the SHAM group maintained an intact spinal cord structure, whereas the SCI group exhibited severe injury. The PLA+GO+Ab group demonstrated a significant reduction in SCI severity and better spinal cord reconnection. (**C**) Quantification of cavity area in spinal cord tissue based on H&E staining indicated that the PLA+GO+Ab group significantly reduced the cavity area in the SCI region, showing a marked improvement compared to other groups. (**D**) Histological analysis of H&E staining revealed severe tissue damage and cellular degeneration in the SCI group, whereas the PLA+GO+Ab group exhibited better spinal cord structure preservation and cellular repair, further demonstrating the role of the composite scaffold in promoting SCI recovery. (**E**) Compared to the SCI group, the PLA+GO+Ab group exhibited significantly increased expression of GAP43, a key nerve regeneration-related protein, indicating its role in promoting axonal regeneration. (**F**) Quantification of GAP43 expression showed that PLA+GO+Ab significantly upregulated GAP43 levels compared to the SCI group and also exhibited a notable increase relative to the PLA+Ab group, suggesting a stronger effect in promoting axonal regeneration. (**G**) qRT-PCR analysis demonstrated that, compared to the SCI group, the PLA+GO+Ab group significantly down-regulated RGMA expression (a negative regulator of axonal regeneration) and upregulated MAP2 expression (a positive regulator for axonal regeneration), further confirming the potential therapeutic role of the PLA+GO+Ab composite scaffold in promoting spinal cord repair and axonal regeneration. (n=8) (***P<0.001, ****P<0.0001).

Compared to other groups, PLA+GO+Ab significantly reduced CD86 ($P < 0.01$) expression while enhancing CD206 expression ($P < 0.001$), suggesting a shift toward M2 polarization and an improved regenerative microenvironment.

Additionally, we utilized flow cytometry to analyze CD86 and CD206 expression in spinal cord tissue (Figure 7C). Flow cytometry analysis of CD86+ (M1) and CD206+ (M2) macrophages to quantify immune cell polarization across different groups. The SCI group showed a higher percentage of CD86+ macrophages and a lower percentage of CD206+ macrophages, consistent with a persistent inflammatory state. The groups treated with Ab-containing materials (PLA+Ab and PLA+GO+Ab) exhibited a significant reduction in M1 macrophages and an increase in M2 macrophages, indicating that Ab incorporation effectively promotes M2 polarization. Furthermore, compared to the PLA+Ab group, the PLA+GO

https://doi.org/10.2147/IJN.S509954

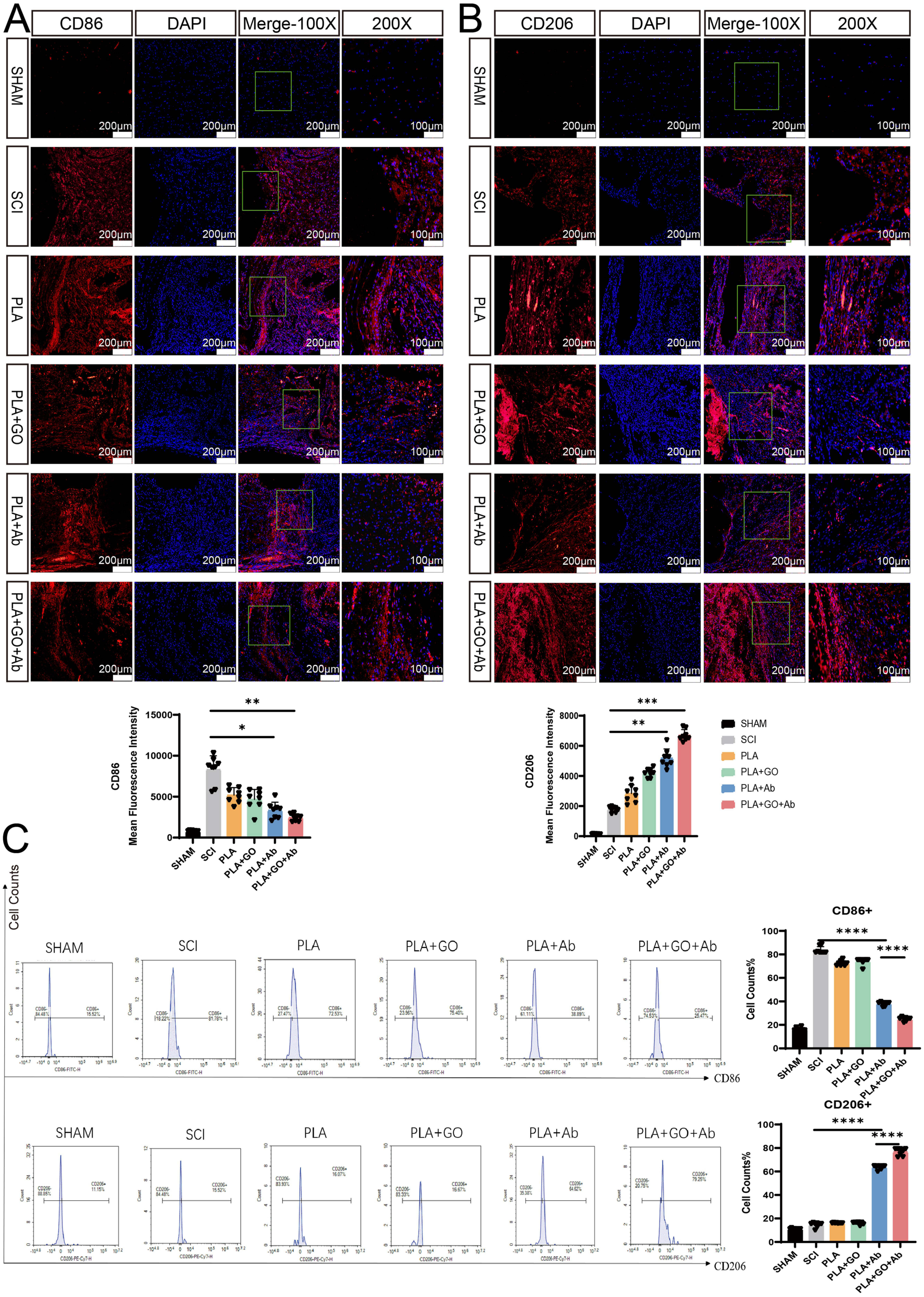

Figure 7 Effects of Composite Scaffolds on Macrophage Polarization in vivo. (**A** and **B**) Immunofluorescence staining of CD86 (M1 marker, (**A**)) and CD206 (M2 marker, (**B**)) in spinal cord tissues. The SCI group exhibited a high expression of CD86+ M1 macrophages, while the PLA+GO+Ab group significantly reduced CD86 expression and increased CD206+ M2 macrophages, indicating a shift toward an anti-inflammatory phenotype. (**C**) Flow cytometry analysis quantifying the proportion of CD86+ (M1) and CD206+ (M2) macrophages in different groups. The PLA+GO+Ab group exhibited the lowest proportion of CD86+ M1 macrophages and the highest proportion of CD206+ M2 macrophages, confirming that the composite scaffold promotes M2 polarization and reduces inflammation. These results demonstrate that PLA+GO+Ab enhances macrophage polarization toward an anti-inflammatory M2 phenotype, which may contribute to spinal cord repair. (n=8) (*P < 0.05, **P < 0.01, ***P < 0.001, ****P < 0.0001).

+Ab group demonstrated a significantly greater enhancement of M2 macrophage polarization ($P < 0.0001$), suggesting that GO further enhances the immunoregulatory effects of Ab.

In vivo Effects of Composite Scaffold on Promotion of Neural Differentiation and Oligodendrocyte Progenitor Cells

Based on the observed functional recovery in animal models, we further investigated the effects of PLA+GO+Ab on neuronal regeneration and oligodendrocyte maturation in spinal cord tissue. The expression of βIII-tubulin (βIII), a neuronal marker, was significantly increased in the PLA+GO+Ab group compared to the SCI group (Figure 8A and C), this suggests that PLA+GO+Ab supports neuronal regeneration in the injured spinal cord. Additionally, since axonal regeneration depends on the interaction between axons and oligodendrocytes, we further analyzed the role of OPCs in this process. To assess oligodendrocyte maturation, we examined NG2, PDGFRα, and A2B5, which are markers of different OPC developmental stages. NG2, an early OPC marker, was significantly decreased in the PLA+GO+Ab group (Figure 8B and C), suggesting that OPCs were progressing to a more differentiated state. Correspondingly, PDGFRα, a marker of more mature OPCs, was significantly upregulated in the PLA+GO+Ab group (Figure 9A and C), indicating enhanced oligodendrocyte differentiation. Additionally, A2B5, a marker associated with glial progenitor cells, also showed a significant increase in the PLA+GO+Ab group (Figure 9B and C), further supporting the promotion of OPC differentiation and maturation. These findings suggest that PLA+GO+Ab not only enhances neuronal regeneration but also facilitates OPC maturation, potentially contributing to axonal remyelination and improved functional recovery following spinal cord injury.

Discussion

SCI is a severe condition causing significant neurological deficits with limited treatment options.[27] This study developed a PLA+GO+Ab composite to regulate immune responses and promote neurological recovery after SCI. In this study, we first investigated the advantages of incorporating anti-TNF-α into the PLA+GO composite through co-electrospinning. Unlike traditional surface-coating methods that may lead to uneven distribution and rapid degradation, our approach ensures uniform dispersion of the antibody within the PLA+GO matrix, providing prolonged bioactivity and a controlled immune-modulatory effect. Compared with conventional drug-loading strategies such as post-fabrication swelling methods, which rely on material immersion in drug solutions for absorption, our method avoids uneven drug distribution and burst release issues.[28] The electrospinning process allows for more controlled and homogeneous drug incorporation within the fibers, enhancing sustained release and bioavailability.

To further validate the effectiveness of our approach, we analyzed the surface charge properties and drug release behavior of the composite. Zeta potential measurements demonstrated that the incorporation of anti-TNF-α altered the surface charge properties of the composite, leading to a reduction in negative charge. Since antibodies are proteins with positively charged regions, this shift in surface potential suggests the successful introduction of anti-TNF-α. The decrease in negative charge may influence cellular interactions by reducing electrostatic repulsion between the composite and cells, potentially facilitating a more favorable environment for cellular adhesion within the acidic microenvironment of SCI. This change in surface charge also indirectly confirms the successful incorporation of the antibody into the composite. Additionally, ELISA confirmed the sustained and stable release of the anti-TNF-α antibody, ensuring long-term immunomodulatory effects at the injury site. Our results indicate that this approach enables stable antibody release while also modifying the composite's surface properties, potentially optimizing its interactions with the biological environment and providing an effective strategy for immune modulation and neural repair in SCI treatment.

To evaluate the impact of GO incorporation on the physicochemical properties of PLA, multiple characterization techniques were employed. SEM demonstrated a uniform dispersion of GO within the PLA matrix without noticeable agglomeration, confirming effective integration. FTIR and XPS analyses revealed that GO introduced oxygen-containing functional groups, modifying the surface chemistry of the composite without altering its fundamental molecular structure. Raman spectroscopy further confirmed the presence of GO through characteristic D and G bands, indicating the presence of graphitic structures and defect sites that may contribute to improved cell interactions.[29–31] XRD analysis showed the

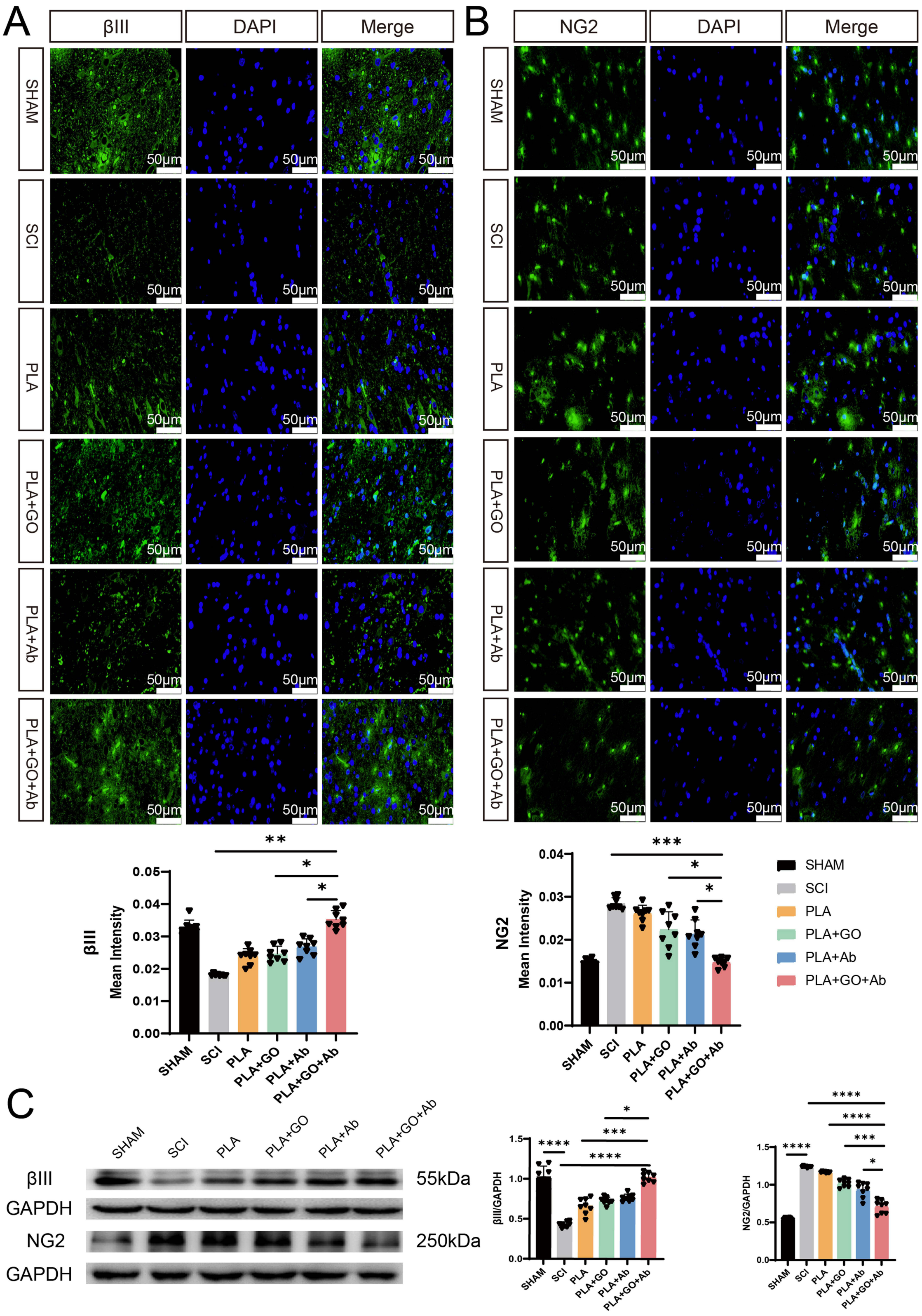

Figure 8 Effects of Composite Scaffolds on Neuronal Regeneration and Oligodendrocyte Differentiation. (**A** and **B**) Immunofluorescence staining of βIII-tubulin and NG2 in spinal cord tissues. Compared to the SCI group, the PLA+GO+Ab group exhibited significantly increased βIII expression ($P < 0.01$), indicating enhanced neuronal regeneration. Meanwhile, NG2 expression was reduced, suggesting a shift from early-stage oligodendrocyte progenitors toward more mature oligodendrocytes ($P < 0.001$). (**C**) Western blot analysis of βIII and NG2 protein expression confirmed the immunofluorescence results, showing that PLA+GO+Ab significantly increased βIII expression while reducing NG2 expression, further supporting its role in promoting neuronal regeneration and oligodendrocyte differentiation. (n=8) (*$P<0.05$, **$P<0.01$, ***$P<0.001$, ****$P<0.0001$).

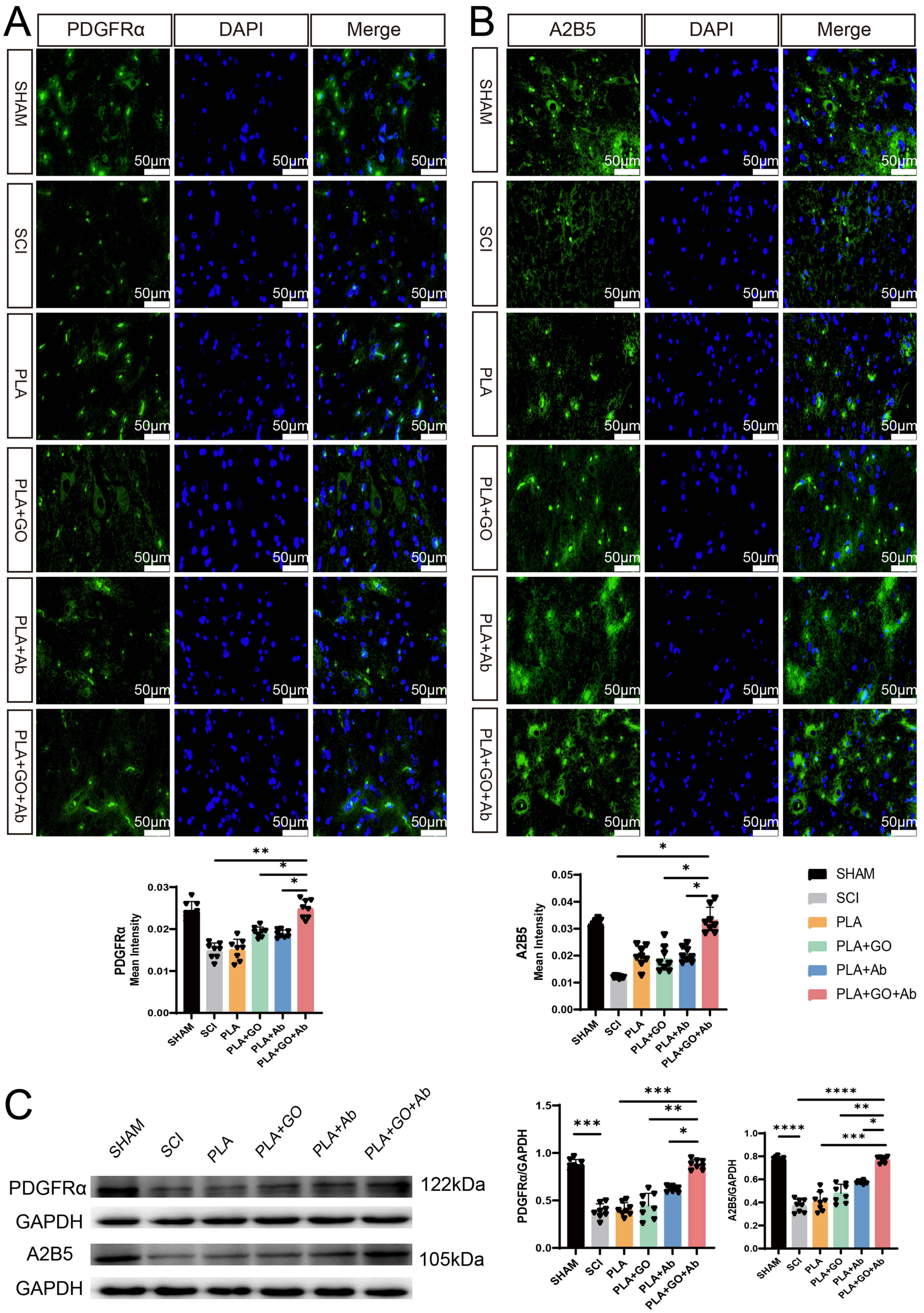

Figure 9 Effects of Composite Scaffolds on Oligodendrocyte Maturation in Spinal Cord Injury. (**A** and **B**) Immunofluorescence staining of PDGFRα and A2B5, markers of oligodendrocyte progenitor cells, in spinal cord tissues. NG2 is an early-stage OPC marker, while PDGFRα and A2B5 represent more mature oligodendrocyte precursors. The PLA+GO+Ab group exhibited significantly increased PDGFRα ($P < 0.01$) and A2B5 ($P < 0.05$) expression, suggesting that the scaffold promotes the maturation of OPCs into functional oligodendrocytes. (**C**) Western blot analysis of PDGFRα and A2B5 protein expression further validated the immunofluorescence findings, showing that PLA+GO+Ab significantly upregulated OPC marker expression, supporting its role in enhancing oligodendrocyte differentiation and maturation. (n=8) (*$P<0.05$, **$P<0.01$, ***$P<0.001$, ****$P<0.0001$).

emergence of a diffraction peak at 2θ ≈ 26.5°, corresponding to the (002) plane of graphite,[30,32] suggesting that GO maintains an ordered structure within the PLA matrix and influences its molecular arrangement. Collectively, these results indicate that the addition of GO enhances the surface chemistry, structural integrity, and bioactivity of the composite while preserving its overall polymeric framework.

GO has been shown to promote NSC adhesion, proliferation, and endogenous migration,[33] which is critical for effective SCI repair. RNA sequencing further revealed that GO influenced key signaling pathways in NSCs, particularly the Rap1 signaling pathway, which orchestrates multiple downstream networks such as PI3K-Akt, ERK/MAPK, and cytoskeletal regulatory pathways. Rap1 has been identified as a crucial factor in neural development,[34] injury repair, and tissue regeneration, reinforcing the mechanistic foundation for the enhanced functional recovery observed in our study. However, while PLA+GO demonstrated strong pro-migratory effects in vitro, its in vivo efficacy was limited due to the harsh immune microenvironment after SCI, which hindered NSC recruitment and integration. In contrast, PLA+Ab effectively improved the immune environment but lacked the structural and biochemical support needed for optimal NSC migration and differentiation. Notably, PLA+GO+Ab exhibited the most significant enhancement in NSC migration at 14 days post-SCI, a critical period during the chronic inflammatory phase. This suggests that GO's ability to promote NSC migration was maximized only when coupled with inflammation regulation by anti-TNF-α, ensuring a permissive microenvironment for neural repair. The superior performance of PLA+GO+Ab confirms that neither GO nor anti-TNF-α alone was sufficient for optimal recovery, highlighting the necessity of a combined approach to simultaneously regulate the immune response and enhance cellular migration.

Hence, neuronal differentiation and regeneration require an optimal immune microenvironment, characterized by minimal inflammatory activity and a well-regulated immune response that supports tissue repair. In the absence of a favorable immune microenvironment, simply promoting the migration and proliferation of NSCs cannot achieve the desired effect. Many current biomaterial-based SCI treatment strategies, such as collagen scaffolds and various stem cell therapies, focus on promoting M2 macrophage polarization and reducing pro-inflammatory cytokine release to alleviate inflammation.[35–37] While these approaches can help mitigate secondary inflammatory damage, they are primarily reactive interventions—addressing inflammation only after it has already caused damage to neural tissues. Consequently, although these treatments improve the immune microenvironment and contribute to SCI repair, they fail to eliminate pre-existing inflammatory accumulations, leaving unresolved issues of persistent pro-inflammatory cytokines and immune cell infiltration, which continue to hinder long-term neural regeneration.

To overcome the detrimental effects of excessive TNF-α on neural repair,[38] we proposed a "depletion" strategy that not only mitigates inflammation but actively neutralizes and clears excess inflammatory cytokines at the injury site. By integrating anti-TNF-α antibodies into the PLA+GO scaffold, we effectively reduce the overactivation of TNF-α, relieving immune burden and shifting the immune balance towards a pro-regenerative M2 macrophage phenotype while decreasing M1 pro-inflammatory macrophage populations. This dual intervention not only suppresses newly emerging inflammatory responses but also eliminates existing inflammatory infiltrates, providing a more stable and favorable immune environment for neural regeneration. As expected, ELISA demonstrated that the presence of anti-TNF-α effectively reduced TNF-α levels in the culture medium, while flow cytometry confirmed a shift in macrophage polarization—decreasing M1 macrophages and increasing M2 macrophages. This transition is critical, as M2 macrophages contribute to a more reparative microenvironment that facilitates oligodendrocyte maturation, a crucial step in myelin regeneration and axonal recovery. Myelin restoration is essential for proper neuronal function, as it enhances axonal conductivity and supports long-term neuroprotection.[39] The PLA+GO+Ab composite not only improved immune homeostasis but also enhanced oligodendrocyte differentiation, promoting faster maturation of oligodendrocyte precursors.

Nonetheless, while our study primarily explored the role of GO in regulating NSC behavior, the specific mechanisms by which anti-TNF-α modulates macrophage polarization remain incompletely understood. Future research should focus on elucidating the molecular pathways involved in this process and identifying additional factors that may enhance macrophage-driven neuroprotection. Understanding these mechanisms could further refine biomaterial-based immunotherapy strategies, optimizing SCI treatment outcomes.

Conclusion

This study demonstrates that the PLA+GO+Ab composite effectively promotes neural repair and immune regulation after spinal cord injury. The composite enhances NSC proliferation, migration, and differentiation by activating the Rap1 signaling pathway, while also inducing M2 macrophage polarization, reducing inflammation, and improving motor function recovery. These findings highlight PLA+GO+Ab as a promising biomaterial for SCI treatment, warranting further research to optimize its clinical application.

Data Sharing Statement

The data can be obtained from the corresponding author upon reasonable request.

Ethics Approval

All procedures were performed following the National Institutes of Health (NIH) Guidelines for the Care and Use of Laboratory Animals (1996). The experiments were approved by the Animal Care and Use Committee of The First Hospital Affiliated to Harbin Medical University (No. 2020052).

Acknowledgments

This study was supported by the Natural Science Foundation of China (Project No. 81871781) and Key Project of Natural Science Foundation of Heilongjiang Province of China (Project No. ZD2021H003).

Disclosure

The authors declare that they have no competing interests in this work.

References

1. Eckert MJ, Martin MJ. Trauma: spinal cord injury. *Surg Clin North Am*. 2017;97(5):1031–1045. doi:10.1016/j.suc.2017.06.008
2. Sweis R, Biller J. Systemic complications of spinal cord injury. *Curr Neurol Neurosci Rep*. 2017;17(2):8. doi:10.1007/s11910-017-0715-4
3. Lund MC, Clausen BH, Brambilla R, Lambertsen KL. The role of tumor necrosis factor following spinal cord injury: a systematic review. *Cell Mol Neurobiol*. 2023;43(3):925–950. doi:10.1007/s10571-022-01229-0
4. Jiang Z, Zeng Z, He H, et al. Lycium barbarum glycopeptide alleviates neuroinflammation in spinal cord injury via modulating docosahexaenoic acid to inhibiting MAPKs/NF-kB and pyroptosis pathways. *J Transl Med*. 2023;21(1):770. doi:10.1186/s12967-023-04648-9
5. Su X, Jing X, Jiang W, et al. Curcumin-containing polyphosphazene nanodrug for anti-inflammation and nerve regeneration to improve functional recovery after spinal cord injury. *Int J Pharm*. 2023;642:123197. doi:10.1016/j.ijpharm.2023.123197
6. Esposito E, Cuzzocrea S. Anti-TNF therapy in the injured spinal cord. *Trends Pharmacol Sci*. 2011;32(2):107–115. doi:10.1016/j.tips.2010.11.009
7. Lund MC, Ellman DG, Nissen M, et al. The inflammatory response after moderate contusion spinal cord injury: a time study. *Biology*. 2022;11(6):939. doi:10.3390/biology11060939
8. Qian D, Xu J, Zhang X, et al. Microenvironment self-adaptive nanomedicine promotes spinal cord repair by suppressing inflammation cascade and neural apoptosis. *Adv Mater*. 2024;36(50):e2307624. doi:10.1002/adma.202307624
9. Yu H, Yang S, Li H, Wu R, Lai B, Zheng Q. Activating endogenous neurogenesis for spinal cord injury repair: recent advances and future prospects. *Neurospine*. 2023;20(1):164–180. doi:10.14245/ns.2245184.296
10. Wu Y, Tang Z, Zhang J, Wang Y, Liu S. Restoration of spinal cord injury: from endogenous repairing process to cellular therapy. *Front Cell Neurosci*. 2022;16:1077441. doi:10.3389/fncel.2022.1077441
11. Fu H, Hu D, Chen J, et al. Repair of the injured spinal cord by Schwann cell transplantation. *Front Neurosci*. 2022;16:800513. doi:10.3389/fnins.2022.800513
12. Xue J, Wu T, Dai Y, Xia Y. Electrospinning and electrospun nanofibers: methods, materials, and applications. *Chem Rev*. 2019;119(8):5298–5415. doi:10.1021/acs.chemrev.8b00593
13. Garg K, Bowlin GL. Electrospinning jets and nanofibrous structures. *Biomicrofluidics*. 2011;5(1):13403. doi:10.1063/1.3567097
14. Agarwal G, Roy A, Kumar H, Srivastava A. Graphene-collagen cryogel controls neuroinflammation and fosters accelerated axonal regeneration in spinal cord injury. *Biomater Adv*. 2022;139:212971. doi:10.1016/j.bioadv.2022.212971
15. Girão AF, Serrano MC, Completo A, Marques PAAP. Is graphene shortening the path toward spinal cord regeneration? *ACS Nano*. 2022;16(9):13430–13467. doi:10.1021/acsnano.2c04756
16. Wang S-X, Lu Y-B, Wang -X-X, et al. Graphene and graphene-based materials in axonal repair of spinal cord injury. *Neural Regen Res*. 2022;17(10):2117–2125. doi:10.4103/1673-5374.335822
17. Georgakilas V, Otyepka M, Bourlinos AB, et al. Functionalization of graphene: covalent and non-covalent approaches, derivatives and applications. *Chem Rev*. 2012;112(11):6156–6214. doi:10.1021/cr3000412
18. Kolahdouz M, Xu B, Nasiri AF, et al. Carbon-related materials: graphene and carbon nanotubes in semiconductor applications and design. *Micromachines*. 2022;13(8). doi:10.3390/mi13081257

19. Magne TM, de Oliveira Vieira T, Alencar LMR, et al. Graphene and its derivatives: understanding the main chemical and medicinal chemistry roles for biomedical applications. *J Nanostruct Chem*. 2022;12(5):693–727. doi:10.1007/s40097-021-00444-3
20. Patil R, Bahadur P, Tiwari S. Dispersed graphene materials of biomedical interest and their toxicological consequences. *Adv Colloid Interface Sci*. 2020;275:102051. doi:10.1016/j.cis.2019.102051
21. Holt BD, Wright ZM, Arnold AM, Sydlik SA. Graphene oxide as a scaffold for bone regeneration. *Wiley Interdiscip Rev Nanomed Nanobiotechnol*. 2017;9(3). doi:10.1002/wnan.1437
22. Yang B, Wang P-B, Mu N, et al. Graphene oxide-composited chitosan scaffold contributes to functional recovery of injured spinal cord in rats. *Neural Regen Res*. 2021;16(9):1829–1835. doi:10.4103/1673-5374.306095
23. Basso DM, Beattie MS, Bresnahan JC. A sensitive and reliable locomotor rating scale for open field testing in rats. *J Neurotrauma*. 1995;12(1):1–21. doi:10.1089/neu.1995.12.1
24. Hellenbrand DJ, Quinn CM, Piper ZJ, Morehouse CN, Fixel JA, Hanna AS. Inflammation after spinal cord injury: a review of the critical timeline of signaling cues and cellular infiltration. *J Neuroinflammation*. 2021;18(1):284. doi:10.1186/s12974-021-02337-2
25. Alibardi L. Growth associated protein 43 and neurofilament immunolabeling in the transected lumbar spinal cord of lizard indicates limited axonal regeneration. *Neural Regen Res*. 2022;17(5):1034–1041. doi:10.4103/1673-5374.324850
26. Isaksen TJ, Fujita Y, Yamashita T. Repulsive guidance molecule A suppresses adult neurogenesis. *Stem Cell Rep*. 2020;14(4):677–691. doi:10.1016/j.stemcr.2020.03.003
27. Anjum A, Yazid MD, Fauzi Daud M, et al. Spinal cord injury: pathophysiology, multimolecular interactions, and underlying recovery mechanisms. *Int J Mol Sci*. 2020;21(20):7533. doi:10.3390/ijms21207533
28. Mirzaie Z, Reisi-Vanani A, Barati M, Atyabi SM. The drug release kinetics and anticancer activity of the GO/PVA-curcumin nanostructures: the effects of the preparation method and the GO amount. *J Pharm Sci*. 2021;110(11):3715–3725. doi:10.1016/j.xphs.2021.07.016
29. Le HN, Nguyen TBY, Nguyen DTT, Dao TBT, Nguyen TD, Ha thuc CN. Sonochemical synthesis of bioinspired graphene oxide-zinc oxide hydrogel for antibacterial painting on biodegradable polylactide film. *Nanotechnology*. 2024;35(30):305601. doi:10.1088/1361-6528/ad40b8
30. Wang Y, Li C, Wang T, Li X, Li X. Polylactic acid-graphene oxide-based materials for loading and sustained release of poorly soluble pesticides. *Langmuir*. 2020;36(41):12336–12345. doi:10.1021/acs.langmuir.0c02320
31. Laraba SR, Ullah N, Bouamer A, et al. Enhancing structural and thermal properties of Poly(lactic acid) using graphene oxide filler and anionic surfactant treatment. *Molecules*. 2023;28(18):6442. doi:10.3390/molecules28186442
32. Jevtovic V, Khan AU, Almarhoon ZM, et al. Synthesis of MnSe-based GO composites as effective photocatalyst for environmental remediations. *Nanomaterials*. 2023;13(4):667. doi:10.3390/nano13040667
33. Stenudd M, Sabelström H, Frisén J. Role of endogenous neural stem cells in spinal cord injury and repair. *JAMA Neurol*. 2015;72(2):235–237. doi:10.1001/jamaneurol.2014.2927
34. Kooistra MRH, Dubé N, Bos JL. Rap1: a key regulator in cell-cell junction formation. *J Cell Sci*. 2007;120(Pt 1):17–22. doi:10.1242/jcs.03306
35. Chen S, Saeed AFUH, Liu Q, et al. Macrophages in immunoregulation and therapeutics. *Signal Transduct Target Ther*. 2023;8(1):207. doi:10.1038/s41392-023-01452-1
36. Gordon S, Martinez-Pomares L. Physiological roles of macrophages. *Pflugers Arch*. 2017;469(3–4):365–374. doi:10.1007/s00424-017-1945-7
37. Xia T, Fu S, Yang R, et al. Advances in the study of macrophage polarization in inflammatory immune skin diseases. *J Inflamm*. 2023;20(1):33. doi:10.1186/s12950-023-00360-z
38. Cui X, Huang C, Huang Y, et al. Amplification of metalloregulatory proteins in macrophages by bioactive ZnMn@SF hydrogels for spinal cord injury repair. *ACS Nano*. 2024;18(49):33614–33628. doi:10.1021/acsnano.4c12236
39. Pukos N, Goodus MT, Sahinkaya FR, McTigue DM. Myelin status and oligodendrocyte lineage cells over time after spinal cord injury: what do we know and what still needs to be unwrapped? *Glia*. 2019;67(11):2178–2202. doi:10.1002/glia.23702